A Nonlinear Model of an Ocean Driven by Wind and Differential Heating: Part I. Description of the Three-Dimensional Velocity and Density Fields

KIRK BRYAN AND MICHAEL D. COX

Geophysical Fluid Dynamics Laboratory, ESSA, Princeton, N. J.

(Manuscript received 1 May 1967, in revised form 1 June 1968)

ABSTRACT

A numerical experiment is carried out to investigate the circulation of an ocean, driven by a prescribed density gradient and wind stress at the surface. The mathematical formulation includes in one model most of the physical effects that have been considered in previous theoretical studies. Starting out from conditions of uniform stratification and complete rest, an extensive numerical integration is carried out with respect to time. Care is taken in the final stages of the calculation to use a finite difference net which resolves the very narrow boundary layers which form along the side walls of the basin.

A detailed description is made of the three-dimensional velocity and temperature patterns obtained from the final stage of the run. Since inertial effects play an important role in the western boundary current, it is possible to verify with a baroclinic model two results obtained previously with barotropic ocean models: 1) a concentrated outflow from the western boundary takes place along the upper boundary of the subtropic wind gyre; and 2) inertial recirculation may increase the total transport of the boundary current to a value well above that given by linear theory. In addition to the western boundary current, a strong eastward flowing current is found along the equator. Taking into account a difference in Rossby number between model and prototype, the intensity of the computed currents agrees very closely to observations in the Gulf Stream and the Equatorial Current.

1. Introduction

The problem of the large-scale circulation of the ocean driven by differential heating and mechanical stresses exerted by wind at the surface has been the subject of many investigations, dating back to the 18th century. Several different flow regimes occur in the time-averaged flow within a typical basin. In particular, there is a striking difference between the intense western boundary currents of the Northern Hemisphere oceans and the type of flow over the rest of the basin. These differences, in addition to the complex geometry of actual ocean basins, make the ocean circulation very difficult to treat using conventional analytic methods.

The present knowledge of the dynamics of the large-scale motions is based largely on studies undertaken in the last two decades. A comprehensive review of current progress in this field is given by Stommel (1965) in *The Gulf Stream*. A basic difficulty encountered in recent studies is that it has been relatively easy to formulate relevant mathematical models for the study of large-scale ocean circulation, but very difficult to find solutions. Some insight has been gained through the study of hydrodynamic experiments, and much remains to be done in this promising field of research. In addition, the physics of large-scale flow in the ocean has much in common with large-scale flow in the atmosphere. This suggests that the direct computational approach based on the hydrodynamic equations which has been successfully applied in studies of the atmospheric general circulation (Phillips, 1956; Smagorinsky, 1963) can be carried over to the study of the oceans. Pioneering work along these lines has been carried out by Sarkisyan (1954, 1962) and Gormatyuk and Sarkisyan (1965) in the Soviet Union. Studies of barotropic models also based on a numerical method have been made by Bryan (1963), Fischer (1965) and Veronis (1966) in the United States.

The present investigation is an extension of a series of calculations for a baroclinic ocean model by the authors (Bryan and Cox, 1967), hereafter referred to as A. A motivation for study A was a controversy, which has existed for over a century, as to whether wind or differential heating is the primary factor in driving the ocean circulation. Up to the present these two factors usually have been treated separately. Implicit in the thinking of many oceanographers about the ocean circulation is a linear superposition of two solutions, one based on thermocline theory, and the other based on wind-driven theory. Due to important nonlinearities that exist in the more general mathematical models of large-scale ocean currents, such a superposition is not strictly valid. In study A an attempt was therefore made to include in one model the various factors that had been treated separately in previous studies.

The results of A indicated that qualitatively many features of the Northern Hemisphere ocean basins could be explained on the basis of a model driven by differential heating alone. A weak western boundary current and a well developed thermocline are present, as well as a deep southward drift of surface waters in the subtropical gyre. However, the addition of wind brings the solutions into much better agreement with observations. The topography of the thermocline is changed so that it takes on the characteristic tilt upward to the east which is a striking feature of east-west hydrographic sections in the subtropical gyre of the North Atlantic. The western boundary current is also greatly increased in strength, and the wind pattern provides a mechanism for an outflow from the western boundary current to take place at middle latitudes.

A shortcoming of the calculations of A is that, due to computational limitations, only rather viscous cases are considered. Nonlinear effects are important in determining the density field, but not in the transfer of momentum. The present study is a detailed investigation of a single numerical experiment in which the parameters are chosen so that inertial effects are really significant in the western boundary. This allows a comparison with the nonlinear wind-driven calculations based on simpler barotropic models. As the three-dimensional velocity and density fields are very difficult to describe, attention is focused on a single numerical experiment. In Part II of this investigation (Bryan and Cox, 1968) the solution is analyzed in some detail to determine the vorticity and heat balance of both the interior and boundary current regions.

2. Equations of the model

Except for certain details, the equations of the mathematical model and the numerical method are the same as that used in the previous investigation A. In order that the present paper may be read independently, however, a brief description of the model is given in this section. The numerical scheme will be given in the following section.

The principal approximations are: 1) assumption of hydrostatic balance; 2) neglect of density variations, except where they occur as a coefficient of the gravitational constant; and 3) the replacement of molecular viscosity and diffusion with new terms representing "turbulent" viscosity and diffusion due to scales of motion too small to be resolved by the numerical grid. These approximations are discussed by Fofonoff (1962). The first two may be shown to be quite accurate for the study of ocean circulation problems. Since very little is known about the turbulence characteristics of the ocean, the third assumption is less certain. Let

$$D''(\ )=(\ )_t+\frac{u''}{a\cos\varphi}(\ )_\lambda+\frac{v''}{a}(\ )_\varphi+w''(\ )_z, \quad (2.1)$$

where λ is longitude, φ latitude, a the earth's radius, and

$$u''=a\cos\varphi\,\dot{\lambda}, \quad (2.2)$$

$$v''=a\dot{\varphi}, \quad (2.3)$$

$$w''=\dot{z}''. \quad (2.4)$$

With this notation the momentum equations are:

$$D''u''-\left(2\Omega\sin\varphi+u''\frac{\tan\varphi}{a}\right)v''=-\frac{1}{a\cos\varphi}(p/\rho_0)_\lambda''+F^{\lambda''}+\kappa u_{zz}'' \quad (2.5)$$

(double primes being understood where z and t are used as subscripts),

$$D''v''+\left(2\Omega\sin\varphi+u''\frac{\tan\varphi}{a}\right)u''=-\frac{1}{a}(p/\rho_0)_\varphi''+F^{\varphi''}+\kappa v_{zz}'', \quad (2.6)$$

$$g(1-\alpha\vartheta'')=-(p/\rho_0)_z''. \quad (2.7)$$

The equation of continuity is

$$w_z+\frac{\sec\varphi}{a}[u_\lambda''+(v''\cos\varphi)_\varphi]=0. \quad (2.8)$$

The change ϑ'' in apparent temperature is

$$D''\vartheta''=Q''+\frac{\kappa}{\delta}\vartheta_{zz}''. \quad (2.9)$$

In anticipation of scaling, dimensioned variables are denoted with double primes. The effect of the horizontal components of turbulent viscosity and diffusion are indicated by $F^{\lambda''}$, $F^{\varphi''}$, and Q'', i.e.,

$$F^{\lambda''}=\frac{A_M}{a^2}\left[\Delta u''+(1-\tan^2\varphi)u''-\frac{2\tan\varphi}{\cos\varphi}v_\lambda''\right], \quad (2.10)$$

$$F^{\varphi''}=\frac{A_M}{a^2}\left[\Delta v''+(1-\tan^2\varphi)v''+\frac{2\tan\varphi}{\cos\varphi}u_\lambda''\right], \quad (2.11)$$

$$Q=\frac{A_H}{a^2}\Delta\vartheta'', \quad (2.12)$$

where

$$\Delta=\sec^2\varphi(\ )_{\lambda\lambda}+\sec\varphi[\cos\varphi(\ )_\varphi]_\varphi. \quad (2.13)$$

In the model κ is the coefficient of vertical diffusion of both heat and momentum in the case of stable stratification, and A_H and A_M are the coefficients of lateral diffusion of heat and momentum, respectively.

The derivation of the proper form of the viscous terms for a spherical geometry in the nonisotropic case is given by Saint-Guilly (1956). In (2.9), δ introduces the effect of convective processes when the stratification is unstable. Thus,

$$\delta=\begin{cases}1, & \vartheta_z>0\\ 0, & \vartheta_z<0\end{cases}. \tag{2.14}$$

For unstable stratification, vertical mixing becomes effectively infinite. The boundary conditions at the lateral walls of the basin are:

$$\vartheta_\lambda''=u''=v''=0, \quad \lambda=\lambda_1,\lambda_2, \tag{2.15}$$

$$\vartheta_\varphi''=u''=v''=0, \quad \varphi=\Phi_1,\Phi_2. \tag{2.16}$$

In the present calculation the basin is taken to be 45° of longitude across, and extends from the equator to a latitude of 67°. A condition of mirror symmetry at the equator means that calculations only have to be carried out for one hemisphere. At the lower boundary,

$$\vartheta_z''=w=0, \quad z=-H, \tag{2.17a}$$

$$\rho_0\kappa(u_z'',v_z'')=\tau_B^\lambda,\ \tau_B^\varphi. \tag{2.17b}$$

In the numerical experiment most of the calculations are carried out with the condition that the bottom stress components τ_B^λ, τ_B^φ are zero. A short test calculation is also carried out in which τ_B^λ and τ_B^φ were calculated from Ekman theory. Some of the results of this test are shown in Part II.

The boundary conditions specified at the surface are the most important for determining the character of the solutions. Here we have

$$\left.\begin{aligned}\vartheta''&=\theta^* G_1(\varphi)\\ u_z''&=\frac{\tau^*}{\rho_0\kappa}G_2(\varphi)\\ v_z''&=w=0\end{aligned}\right\} z=0, \tag{2.17c}$$

where G_1 and G_2 are simple functions of latitude of order unity. The shape of these functions is shown in Fig. 1. Conditions (2.17c) imply two different driving mechanisms, differential heating and wind. The condition that $w=0$ at the surface is the "rigid lid" approximation. Variations in surface pressure are taken into account, but the kinematic effects of displacements of the free surface are neglected in the continuity equation. The effects is to filter out external gravitational-inertial waves.

The geostrophic relation differentiated with respect to z is

$$2\Omega\sin\varphi u_z''=-\frac{g\alpha}{a}\vartheta_\varphi''.$$

Thus, a scale velocity connected with differential heating may be defined as

$$V^*=\frac{g\alpha\theta^* d}{2\Omega a}, \tag{2.18a}$$

where d is the scale depth of the thermocline.

A scale velocity due to wind is based on the familiar Sverdrup formula for meridional transport,

$$\frac{2\Omega\cos\varphi}{a}\int_{-H}^{0}\rho_0 v\,dz=\mathrm{curl}_z\tau^s. \tag{2.18b}$$

Thus,

$$V^{**}=\frac{\tau^*}{2\Omega d\rho_0}[(G_2)_\varphi]_{\max}, \tag{2.18c}$$

$[(G_2)_\varphi]_{\max}$ being the maximum gradient of G_2, equal to 5.5 for the curve shown in Fig. 1.

To reduce the equations to nondimensional form the following substitutions may be made:

$$u'',\ v'',\ w''=V^*(u,v,dw/a), \tag{2.19}$$

$$z''=dz, \tag{2.20}$$

$$t''=at/V^*, \tag{2.21}$$

$$(p/\rho_0)''=2\Omega V^* aP, \tag{2.22}$$

$$\vartheta''=\theta^*\vartheta. \tag{2.23}$$

Eqs. (2.5)–(2.9) thus become

$$\mathrm{Ro}(Du-\tan\varphi\ uv-u_{zz})=v\sin\varphi-\sec\varphi\ P_\lambda+\mathrm{RoRe}^{-1}F^\lambda, \tag{2.24}$$

$$\mathrm{Ro}(Dv+\tan\varphi\ uu-v_{zz})=-u\sin\varphi-P_\varphi+\mathrm{RoRe}^{-1}F^\varphi, \tag{2.25}$$

$$\vartheta=P_z, \tag{2.26}$$

$$w_z+\sec\varphi[u_\lambda+(v\cos\varphi)_\varphi]=0, \tag{2.27}$$

$$D\vartheta=\frac{1}{\delta}\vartheta_{zz}+\mathrm{P\acute{e}}^{-1}\Delta\vartheta. \tag{2.28}$$

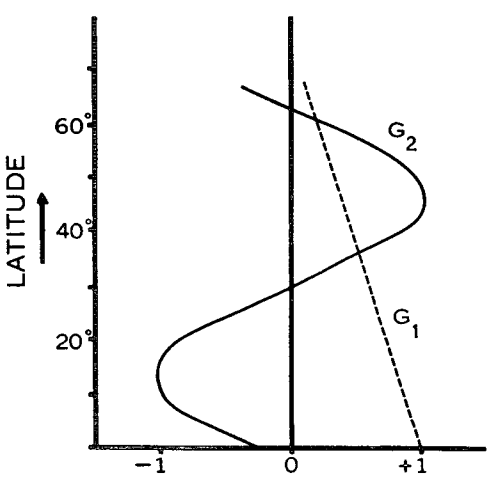

FIG. 1. Temperature distribution and the λ component of the wind stress specified as boundary conditions at the surface.

The above equations have been greatly simplified by setting $D''=V^*D/a$, $d=(\kappa a/V^*)^{\frac{1}{2}}$, and by using the terms,

$$\left.\begin{aligned} F^\lambda &= \Delta u+(1-\tan^2\varphi)u-2\tan\varphi\sec\varphi\, v_\lambda \\ F^\varphi &= \Delta v+(1-\tan^2\varphi)v+2\tan\varphi\sec\varphi\, u_\lambda \end{aligned}\right\}. \quad (2.29)$$

The system (2.24)–(2.28) is governed by 5 parameters. Three appear explicitly in the equations, i.e.,

$$\mathrm{Ro}=V^*/(2\Omega a), \quad (2.30)$$

$$\mathrm{Re}=V^*/A_M, \quad (2.31)$$

$$\mathrm{P\acute{e}}=V^*a/A_H, \quad (2.32)$$

and two others come in through the boundary conditions

$$\gamma=(V^*+V^{**})/V^*, \quad (2.33)$$

$$H/d=\text{total depth/scale depth}. \quad (2.34)$$

Readers not interested in the details of the numerical method may wish to proceed directly to Section 4.

3. Method of calculation

a. Formulation of the finite difference equations

The numerical method makes use of the Mercator projection. If we let

$$\begin{aligned} n&=\sin\varphi, \\ m&=\sec\varphi, \\ dx&=a\,d\lambda, \\ dy&=a\sec\varphi\, d\varphi, \end{aligned}$$

the equations of motion become

$$\frac{du}{dt}-(2\Omega+mu/a)nv-F^x-\kappa u_{zz}=-m(p/\rho_0)_x, \quad (3.1a)$$

$$\frac{dv}{dt}+(2\Omega+mu/a)nu-F^y-\kappa v_{zz}=-m(p/\rho_0)_y. \quad (3.1b)$$

The numerical method will be set down in terms of the unscaled equations of the system. Double primes will be understood on the variables in (3.1a,b) as well as in the remainder of this section. Differentiating (3.1a) and (3.1b) with respect to z, and substituting (2.7), we obtain

$$\left[\frac{du}{dt}-(2\Omega+mu/a)nv-F^x-\kappa u_{zz}\right]_z=-g\alpha m\vartheta_x, \quad (3.2a)$$

$$\left[\frac{dv}{dt}+(2\Omega+mu/a)nu-F^y-\kappa v_{zz}\right]_z=-g\alpha m\vartheta_y. \quad (3.2b)$$

The "rigid lid" approximation given by (2.17c) requires that

$$\int_{-H}^{0}(\nabla\cdot\mathbf{v})dz=0. \quad (3.3)$$

It is possible to define a transport stream function,

$$\int_{-H}^{0}(\rho_0 u,\rho_0 v)dz=-m\Psi_y,\ m\Psi_x, \quad (3.4)$$

which is obtained by first integrating (3.1a) and (3.1b) with respect to z, and dividing the resulting equations by m. If the two integrated equations are cross-differentiated with respect to x and y, we obtain

$$\begin{aligned} \Psi_{xxt}+\Psi_{yyt}=&-\frac{2\Omega}{am^2}\Psi_x \\ &+\int_{-H}^{0}\left\{\left[\left(\frac{du}{dt}-u_t-\frac{1}{a}uvmn-F^x-\kappa u_{zz}\right)m^{-1}\right]_y\right. \\ &\left.-\left[\left(\frac{dv}{dt}-v_t+\frac{1}{a}uumn-F^y-\kappa v_{zz}\right)m^{-1}\right]_x\right\}dz. \end{aligned} \quad (3.5)$$

The finite difference scheme is based on a three-dimensional array of points with indices i, j, k. Where n is used as a superscript, it will indicate the time step. In order to resolve boundary layer phenomena, the grid allows for variable spacing. The coordinates of each grid point are:

$$\left.\begin{aligned} x_2&=\Delta x_2/2 \\ x_i&=x_2+\sum_{l=3}^{i}(\Delta x_l+\Delta x_{l-1})/2, \quad i=3,4,5\cdots \end{aligned}\right\}, \quad (3.6)$$

$$\left.\begin{aligned} y_2&=\Delta y_2/2 \\ y_j&=y_2+\sum_{l=3}^{j}(\Delta y_l+\Delta y_{l-1})/2, \quad j=3,4,5\cdots \end{aligned}\right\}, \quad (3.7)$$

$$\left.\begin{aligned} z_1&=-\Delta z_1/2 \\ z_k&=z_1-\sum_{l=2}^{k}(\Delta z_l+\Delta z_{l-1})/2, \quad k=2,3,4\cdots \end{aligned}\right\}, \quad (3.8)$$

where the points x_1 and y_1 lie outside of the basin.

The arrangement of variables in the vertical is shown in Fig. 2a, where the W values are given along the boundaries between layers. The variables U_k, V_k, T_k, calculated at integral values of k may be thought of as average values for these layers, i.e.,

$$U_k=\frac{1}{\Delta k}\int_{z_{k+\frac{1}{2}}}^{z_{k-\frac{1}{2}}}U dz, \quad (3.9)$$

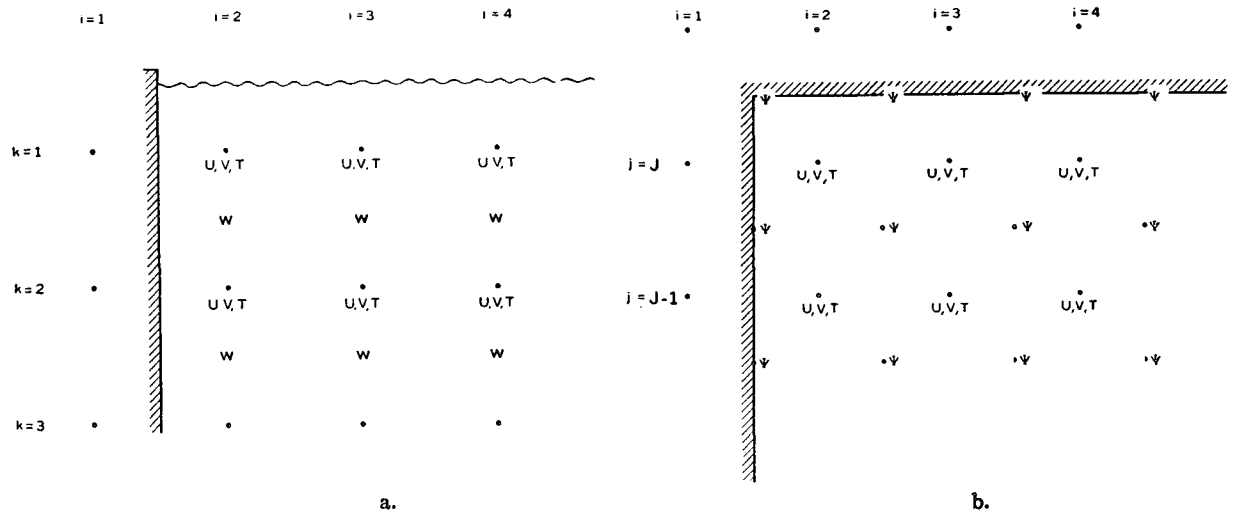

FIG. 2. The arrangement of variables in the vertical plane, a., and horizontal plane, b.

and T_k is the finite difference equivalent of the apparent temperature ϑ. To simplify (3.9) and the remaining equations of this section, Δz_k, Δx_i, and Δy_j will be written as Δk, Δi, Δj, respectively.

In formulating the finite difference equations, the rule adopted for computing U, V and T on the surfaces between the layers is

$$U_{k+\frac{1}{2}}=(U_k+U_{k+1})/2, \tag{3.10}$$

while that for computing derivatives on the surfaces between layers is

$$(U_z)_{k+\frac{1}{2}}=2(U_k-U_{k+1})/(\Delta k+\Delta k+1). \tag{3.11}$$

Within each layer the horizontal transport terms are approximated by the product of vertical averages within the layer. Thus,

$$\frac{1}{\Delta k}\int_{z_{k+\frac{1}{2}}}^{z_{k-\frac{1}{2}}}(VU_y)dz \longrightarrow V_kU_{ky}. \tag{3.12}$$

In writing out the finite difference equations, it is convenient to introduce some shorthand notation for the finite difference operators. As a compromise between an overly cumbersome system and a notation which may be too concise, operations with respect to z and t will be written out in full while horizontal averages and derivatives will be indicated by special symbols.

For this purpose we define:

$$\delta_x(\ )_{i+\frac{1}{2}}=2[(\ )_{i+1}-(\ )_i]/(\Delta i+\Delta i+1), \tag{3.13}$$

$$\bar{\delta}_x(\ )_i=[(\ )_{i+\frac{1}{2}}-(\ )_{i-\frac{1}{2}}]/\overline{\Delta i}^{xx} \tag{3.14}$$

$$\overline{(\ )}^{x}_{i+\frac{1}{2}}=[(\ )_{i+1}+(\ )_i]/2, \tag{3.15}$$

$$\widetilde{(\ )}^{x}_{i+\frac{1}{2}}=[\Delta i+1(\ )_{i+1}+\Delta i(\ )_i]/(\Delta i+1+\Delta i). \tag{3.16}$$

Note that repeated use of these operators may be used to obtain higher derivatives, or three-point averages. For example,

$$\delta_x\delta_x(\ )_i=\{[(\ )_{i+1}-(\ )_i]/\Delta i+\tfrac{1}{2} - [(\ )_i-(\ )_{i-1}]/\Delta i-\tfrac{1}{2}\}/\Delta i, \tag{3.17}$$

$$\overline{(\ )}^{xx}=[(\ )_{i+1}+(\ )_{i-1}+2(\ )_i]/4. \tag{3.18}$$

The horizontal arrangement of variables is given in Fig. 2b, the variables U, V and T being specified at integer grid points.

The temperature equation is represented by the simplest finite difference formula, all indices being i, j, k, n unless otherwise indicated. Thus,

$$T^{n+1}-T^n=\tfrac{3}{2}\Delta tQ^n-\tfrac{1}{2}\Delta tQ^{n-1}, \tag{3.19}$$

where

$$Q^n=-\mathfrak{L}T+\frac{2\kappa}{\Delta k}\left[\frac{(T_{k-1}-T_k)}{\Delta k-1+\Delta k}-\frac{(T_k-T_{k+1})}{\Delta k+\Delta k+1}\right] +A_Hm^2(\delta_x\delta_x+\delta_y\delta_y)T. \tag{3.20}$$

In the description of the model it is specified that

$$\frac{\kappa}{\delta}=\begin{cases}\kappa, & T_z>0\\ \infty, & T_z<0\end{cases}. \tag{3.20a}$$

Eq. (3.20) for Q^n only allows for the stable case. The infinite mixing which occurs in the unstable case is included by testing to see if

$$T_{k-1}{}^{n+1}-T_k{}^{n+1}>0 \tag{3.20b}$$

for all k, i.e., let $(T_{k-1}{}^{n+1})'$ and $(T_k{}^{n+1})'$ be corrected estimates of $T_{k-1}{}^{n+1}$ and $T_k{}^{n+1}$, respectively. If this condition on the static stability is not fulfilled,

$$(T_{k-1}{}^{n+1})'=(T_k{}^{n+1})' =\frac{\Delta k-1T_{k-1}{}^{n+1}+\Delta kT_k{}^{n+1}}{\Delta k-1+\Delta k}. \tag{3.20c}$$

After (3.20b) has been used to test all values of k, and corrections have been made according to (3.20c), the entire process is repeated for all k for as many times as is necessary to insure that (3.20b) is satisfied at every point in the water column.

The operator $\mathfrak{L}$ in (3.20) is

$$\mathfrak{L}\mu=m^2\left[\tilde{\delta}_x\left(\frac{\overline{\tilde{U}^{yy}}^{x}}{m}\,\bar{\mu}^{x}\right)+\tilde{\delta}_y\left(\frac{\overline{\tilde{V}^{xx}}^{y}}{m}\,\bar{\mu}^{y}\right)\right]$$
$$+\tfrac{1}{2}[W_{k-\frac{1}{2}}(\mu_{k-1}+\mu_k)-W_{k+\frac{1}{2}}(\mu_k+\mu_{k+1})]/\Delta k. \quad (3.21)$$

As indicated by (3.21) the advection terms have been combined with the continuity equation in order to be written in flux form. As shown by Arakawa (1966), this is necessary to obtain a form which conserves both the average value and the variance of an advected quantity. Arakawa's ideas may be easily extended to an irregular net. The finite difference form of the continuity equation is equivalent to

$$\mathfrak{L}(1)=0. \quad (3.22)$$

Integrating from the top downwards,

$$W_{k+\frac{1}{2}}=m^2\sum_{l=1}^{k}\left[\tilde{\delta}_x\left(\frac{\overline{\tilde{U}^{yy}}^{x}}{m}\right)+\tilde{\delta}_y\left(\frac{\overline{\tilde{V}^{xx}}^{y}}{m}\right)\right]\Delta z_l, \quad (3.23)$$

since $W=0$ at the surface.

The formulae representing (3.1) and (3.2) are more complicated. In this case we have.

$$(U_k-U_{k+1})^{n+1}-(U_k-U_{k+1})^n$$
$$-2\Omega n\Delta t[r(V_k-V_{k+1})^{n+1}+(1-r)(V_k-V_{k+1})^n]$$
$$=(3\Delta t/2)G^n-(\Delta t/2)G^{n-1}, \quad (3.24)$$

$$(V_k-V_{k+1})^{n+1}-(V_k-V_{k+1})^n$$
$$+2\Omega n\Delta t[r(U_k-U_{k+1})^{n+1}+(1-r)(U_k-U_{k+1})^n]$$
$$=(3\Delta t/2)J^n-(\Delta t/2)J^{n-1}, \quad (3.25)$$

where r is a computational parameter which is set equal to $\frac{2}{3}$ in this study. Eqs. (3.24) and (3.25) must be solved simultaneously to obtain $(U_k-U_{k+1})^{n+1}$ and $(V_k-V_{k+1})^{n+1}$ in terms of the variables at previous time levels. This method is preferred for an ocean circulation model because it permits a time step which is long compared to the inertial period (one-half pendulum day).

The terms on the right-hand side are defined by

$$G^n=-mg\alpha\left(\frac{\Delta j}{\overline{\Delta j}^{yy}}\right)(z_k-z_{k+1})\overbrace{\tilde{\delta}_x(T_k+T_{k+1})/2}^{yy}$$
$$+BU_k-BU_{k+1}, \quad (3.26)$$

$$J^n=-mg\alpha\left(\frac{\Delta i}{\overline{\Delta i}^{xx}}\right)(z_k-z_{k+1})\overbrace{\tilde{\delta}_y(T_k+T_{k+1})/2}^{xx}$$
$$+RV_k-RV_{k+1}, \quad (3.27)$$

$$BU=-\mathfrak{L}U+\frac{1}{a}UVmn+\frac{2\kappa}{\Delta k}\left[\frac{U_{k-1}-U_k}{\Delta k-1+\Delta k}-\frac{U_k-U_{k+1}}{\Delta k+\Delta k+1}\right]$$
$$+A_M\left[m^2(\delta_x\delta_x+\delta_y\delta_y)U+\frac{1}{a^2}(1-m^2n^2)U\right.$$
$$\left.-\frac{1}{a^2}2m^2n\delta_x\bar{V}^{x}\right]. \quad (3.28)$$

The expression for RV is similar.

The transport vorticity equation may be written as

$$(\delta_x\delta_x+\delta_y\delta_y)(\Psi^{n+1}-\Psi^n)$$
$$=(3\Delta t/2)E^n-(\Delta t/2)E^{n-1}, \quad (3.29)$$

where

$$E=-(2\Omega/m^2a)\delta_x\bar{\Psi}^{x}$$
$$+\sum_{k=1}^{K}\Delta k\left\{\frac{1}{\overline{\Delta j}^{y}}\delta_x\left(m^{-1}R\overline{V\Delta j}^{yy}\,\frac{\overline{\Delta i}^{xx}}{\Delta i}\right)\right.$$
$$\left.-\frac{1}{\overline{\Delta i}^{x}}\delta_y\left(m^{-1}B\overline{U\Delta i}^{xx}\,\frac{\overline{\Delta j}^{yy}}{\Delta j}\right)\right\}. \quad (3.30)$$

At each time step (3.29) is solved for Ψ^{n+1} by relaxation, a method which could be easily applied to the irregular grid used in the present study. The relation between U, V and Ψ is

$$\overline{\delta_x\Psi}^{y}=\sum_{k=1}^{K}\rho_0V\Delta k/m, \quad (3.31)$$

$$\overline{\delta_y\Psi}^{x}=-\sum_{k=1}^{K}\rho_0U\Delta k/m. \quad (3.32)$$

b. Formulation of the boundary conditions

As shown in Fig. 2b the boundary is taken to coincide with points at which the transport stream function is carried and between points at which the velocity is carried.

At the western boundary the normal component is set equal to zero by

$$U_{1,j}=-U_{2,j}, \quad \bar{U}^{x}=0. \quad (3.33)$$

In computing the advection terms in the momentum and thermal energy equation, the velocity parallel to the boundary is treated as

$$V_{1,j}=V_{2,j}, \quad \bar{V}^{x}=V_{2,j}, \quad (3.34)$$

and is equivalent to a free-slip condition. However, in computing the viscous terms, the boundary value is reset, so that

$$V_{1,j}=-V_{2,j}, \quad \bar{V}^{x}=0, \quad (3.35)$$

this being consistent with the continuous equations. The only reason for using (3.34) is the finite difference form of the advection operator, $\widetilde{(\ )}^{xx}$ and $\widetilde{(\ )}^{yy}$. Because of these operators, pseudopoints outside the boundary are involved in the computation of advection for points lying inside the boundary.

The boundary conditions on U and V for the north and east walls are similar to that on the west wall. Temperature on all walls is set so that the gradient normal to the wall vanishes, i.e.,

$$T_{1,j}=T_{2,j}, \quad \delta_x T=0. \tag{3.36}$$

The transport stream function is simply set to zero at all wall points. At the equator the symmetry condition requires that

$$\left.\begin{aligned} V_{J'+1}&=-V_{J'-1}\\ \Psi_{J'+1}&=-\Psi_{J'-1}\\ (U,T)_{J'+1}&=(U,T)_{J'-1}\end{aligned}\right\}, \tag{3.37}$$

where J' is the latitude index that coincides with the equator.

The procedure used to calculate new values of U, V and T at each time step is to first solve (3.19) to obtain T^{n+1}, and combine (3.24) and (3.25) to obtain new values of $(U_k-U_{k+1})^{n+1}$ and $(V_k-V_{k+1})^{n+1}$. Then (3.29) is used to find Ψ^{n+1}. The transport stream function determines a reference velocity through (3.31) and (3.32), allowing a computation of new values for U^{n+1} and V^{n+1}.

At the lower boundary of the model, the boundary condition is

$$\kappa\frac{U_K-U_{K+1}}{Z_K-Z_{K+1}}=\left\{\begin{matrix}0\\ -(\Omega n\kappa)^{\frac{1}{2}}(U-V)_K\end{matrix}\right\}, \tag{3.38}$$

the second condition being for the bottom friction case. This formula serves to define a fictitious velocity U_{k+1} in terms of the velocity in the lowest layer and the stress at the bottom.

For temperature at the lower boundary we have

$$T_{k+1}=T_k, \tag{3.39}$$

since there is no heat flow through the bottom boundary.

At the surface

$$\kappa\left(\frac{U_0-U_1}{Z_0-Z_1}\right)=\tau^x/\rho_0, \tag{3.40}$$

$$T_0=T^*(y), \tag{3.41}$$

where T_0 and U_0 are the temperature and velocity of fictitious boundary points lying above the surface of the ocean, U_0 being defined in terms of the prescribed stress at the surface. The definition of Z_0 is arbitrary, since variations in this constant will only effect the definition of U_0, but not the momentum flux at the surface. The same argument applies to Z_{k+1}.

In the actual computations the vertical layering is fine enough to resolve the main thermocline, but not fine enough to resolve the relatively shallow planetary boundary layer at the surface. The consequences of this feature of the calculations is discussed in the Appendix through a comparison of continuous solutions based on Ekman profiles with the corresponding solutions based on the finite difference scheme.

c. The energetic properties of the numerical scheme

Let

$$\overline{(\ )}=\frac{1}{H}\int_{-H}^{0}(\ )dz,$$

and $\hat{(\ )}$ indicate a departure from the vertical mean. Also let

$$\{\ \}=\int_0^X\int_0^Y\int_{-H}^{0}(\ )\frac{dzdydx}{m^2}$$

indicate an integral over the entire volume. Then the kinetic energy of the system may be written as

$$\{\mathcal{K}\}=\left\{\frac{1}{2}\frac{m^2}{\rho_0 H^2}(\Psi_x^2+\Psi_y^2)+\rho_0(\hat{u}^2+\hat{v}^2)\right\}, \tag{3.42}$$

and the potential energy as

$$\mathcal{R}=\rho_0(1-\alpha T)gz. \tag{3.43}$$

In the absence of any dissipation or work done, the sum of kinetic and potential energy is conserved. We now let

$$\{\mathcal{R}\}=\sum_{i=2}^{I}\sum_{j=J'}^{J}\sum_{k=1}^{K}\delta_{J'}\rho_0(1-\alpha T)gz_k\frac{\Delta k\overline{\Delta i}^{xx}\,\overline{\Delta j}^{yy}}{m^2}, \tag{3.44}$$

where

$$\delta_{J'}=\left\{\begin{matrix}1, & j\neq J'\\ \frac{1}{2}, & j=J'\end{matrix}\right\},$$

and J' is the index of the equatorial point. Similarly, we let

$$\{\overline{\mathcal{K}}\}=-\tfrac{1}{2}\sum_{i+\frac{1}{2}=2}^{I-1}\sum_{j+\frac{1}{2}=J'}^{J-1}(\rho_0 H)^{-1}\Psi(\delta_x\delta_x+\delta_y\delta_y)\Psi\overline{\Delta i}^{x}\,\overline{\Delta j}^{y}, \tag{3.45}$$

$$\{\hat{\mathcal{K}}\}=\tfrac{1}{2}\sum_{i=2}^{I}\sum_{j=J'}^{J}\sum_{k=1}^{K}\delta_{J'}\rho_0(\hat{U}^2+\hat{V}^2)\Delta k\overline{\Delta i}^{xx}\,\overline{\Delta j}^{yy}/m^2. \tag{3.46}$$

The numerical scheme has been designed to insure that the sum of $\{\mathcal{R}\}$, $\{\overline{\mathcal{K}}\}$ and $\{\hat{\mathcal{K}}\}$ is conserved within the limitations imposed by the method of time-stepping, and the implicit method of treating the Coriolis terms. All energy is exactly accounted for in the conversion from one form of energy to another. This is a valuable

check on the physical consistency of our numerical system, and the reliability of the machine code.

4. Choice of parameters and the time-dependent behavior of the model

a. Scale considerations

One of the goals of the present study is to find a solution for a baroclinic ocean in which the nonlinear terms in the equations of motion are important. Previous studies (Stommel, 1965, p. 207) indicate that inertial effects alter the classical theories of a wind-driven ocean in a significant way, but these results are based on barotropic models. A scale analysis is necessary to make a rational choice of parameters for the present study. For this purpose we will consider the steady-state equations corresponding to (2.24) and (2.25). To find the thickness of the side wall boundary layers, λ will be replaced with a new coordinate λ^*, such that

$$\lambda = L\lambda^*, \tag{4.1}$$

where L is the ratio of the width of the side wall boundary to the radius of the earth.

In what follows L will be determined as a function of the external parameters of the problem. We let

$$\mathrm{Ro} = L^a, \tag{4.2}$$

$$\mathrm{Ro/Re} = L^b, \tag{4.3}$$

$$(\mathrm{P\acute{e}})^{-1} = L^c, \tag{4.3a}$$

where the constants a and b are to be determined from the condition that the boundary current is quasi-geostrophic; that is, the primary balance of the downstream component along the boundary is geostrophic, but inertial and viscous terms are important in the case of the transverse velocity component. The remaining constant c is specified by the condition that near the coast lateral mixing of heat is of the same order as other terms in the heat balance.

In what follows all derivatives with respect to λ will be understood to be derivatives with respect to λ^*. Substituting (4.1)–(4.3a) into (2.24) and (2.25), we obtain

$$L^{a-1}\sec\varphi\, uu_\lambda + L^a(vu_\varphi + wu_z - \tan\varphi\, uv - u_{zz}) = v\sin\varphi - L^{-1}\sec\varphi\, P_\lambda + L^b[L^{-2}\sec^2\varphi\, u_{\lambda\lambda} + \sec\varphi(\cos\varphi\, u_\varphi)_\varphi + \cdots], \tag{4.4}$$

$$L^{a-1}\sec\varphi uv_\lambda + L^a(vv_\varphi + wv_z + \tan\varphi\, uu - v_{zz}) = -u\sin\varphi - P\varphi + L^b[L^{-2}\sec^2\varphi\, v_{\lambda\lambda} + \sec\varphi(\cos\varphi v_\varphi)_\varphi + \cdots]. \tag{4.5}$$

The continuity and thermal equations are

$$\sec\varphi[L^{-1}u_\lambda + (v\cos\varphi)_\varphi] + w_z = 0, \tag{4.6}$$

$$\sec\varphi\, L^{-1}u\vartheta_\lambda + v\vartheta_\varphi + w\vartheta_z - \vartheta_{zz} = L^c[L^{-2}\sec^2\varphi\,\vartheta_{\lambda\lambda} + \sec\varphi(\cos\varphi\,\vartheta_\varphi)_\varphi]. \tag{4.7}$$

Expanding the boundary layer variables in powers of the small parameter L, we then have

$$\left.\begin{aligned} u_b &= u_o + u_1L + u_2L^2 + \cdots \\ v_b &= v_0L^{-1} + v_1 + v_2L + \cdots \\ w_b &= w_0L^{-1} + w_1 + w_2L + \cdots \\ P_b &= P_0 + P_1L + P_2L^2 + \cdots \\ \vartheta_b &= \vartheta_0 + \vartheta_1L + \vartheta_2L^2 + \cdots \end{aligned}\right\}. \tag{4.8}$$

The sum of the interior velocity and the boundary layer velocity must match the boundary conditions. Note that the interior and transverse components of velocity are O(1), while the vertical velocity and the downstream velocity in the boundary layer are of $O(L^{-1})$. This is determined by the continuity equation (4.6).

Substituting (4.8) in (4.4), (4.6) and (4.7), we obtain to $O(L^{-1})$,

$$\sin\varphi\, v_0 = \sec\varphi\, P_{0\lambda}, \tag{4.9}$$

$$\sec\varphi[u_{0\lambda} + (v_0\cos\varphi)_\varphi] + w_{0z} = 0, \tag{4.10}$$

$$u_0\sec\varphi\,\vartheta_{0\lambda} + v_0\vartheta_{0\varphi} + w_0\vartheta_{0z} = L^{c-1}\sec^2\varphi\,\vartheta_{0\lambda\lambda}. \tag{4.11}$$

To O(1) we obtain from (4.5),

$$L^{a-2}(u_0\sec\varphi\, v_{0\lambda} + v_0v_{0\varphi} + w_0v_{0z}) = -u_0\sin\varphi - P_0\varphi + L^{b-3}\sec^2\varphi\, v_{0\lambda\lambda}. \tag{4.12}$$

The conditions specified initially are that the downstream component V_0 is geostrophic, but inertial and viscous effects are primary in determining the transverse component. The latter condition is satisfied if $a=2$ and $b=3$. The condition that lateral mixing is of primary importance adjacent to the boundary is satisfied if $c=1$ in (4.11).

From (4.3) we now have a measure of the boundary layers associated with the external parameters. Thus,

$$\left.\begin{aligned} L_F &= (\mathrm{RoRe^{-1}})^{\frac{1}{2}} \\ L_I &= \mathrm{Ro}^{\frac{1}{2}} \\ L_M &= (\mathrm{P\acute{e}})^{-1} \end{aligned}\right\}, \tag{4.13}$$

where L_F, L_I and L_M are measures of the boundary layers associated with friction, inertia effects and lateral mixing. Thus, L_F is the width of the viscous western boundary current of the Munk-type (see Stommel, 1965, p. 97), L_I is also a familiar feature of the wind-driven ocean theory, and L_M is a new type of boundary layer width which depends on the baroclinic structure and lateral mixing.

We wish to solve for a case in which the inertial effects in the western boundary current are not overwhelmed by lateral mixing. This will only be the case if the inertial width L_I is of the same order as L_M and L_F. In Table 1 the parameters chosen for the present study are compared with a typical case in the previous study *A*.

From Table 1 it can be seen that by choosing a larger Rossby number the inertial width L_I is larger relative

TABLE 1. The parameters of the computation compared with those of Bryan and Cox (1967).

	Present study	Previous study A
Ro	2×10^{-4}	3×10^{-5}
Re	150	8.0
Pé	150	32
$1+V^*/V^{**}$	2	2
H/d	10	13
L_I	0.014	0.006
L_F	0.011	0.019
L_M	0.007	0.031
ΔS†	0.005	

† The spacing of points in the numerical net adjacent to the side wall boundaries in the final stage of the calculation.

to L_F and L_M without making the problem of resolving the boundary current with the numerical grid greater. In the final part of the computation a refined net is used with a spacing of 0.3° or 0.005 rad along the lateral boundaries.

b. *Time scales*

From the adjustment theory for large-scale motions in the ocean it is known that the longer time scales of response in the ocean are associated with the density field. The geostrophic adjustment of the velocity field takes place within a few days or less. For this reason we can get considerable insight into the longer time scales of the system by just looking at the density equation. To compare our nondimensional time scale to real time, a typical scale velocity can be calculated from (2.18a). We thus let $g=10^3$ cm sec^{-2}, $\theta^*=18°$, $\alpha=2.5\times10^{-4}$ deg^{-1}, $2\Omega=1.47\times10^{-4}$ sec^{-1}, $d=4\times10^4$ cm, and $\tau^*=2.1$ dyn cm^{-2}. These parameters give V^* and V^{**} equal to 2 cm sec^{-1}. From (2.21) our nondimensional unit of time is

$$\frac{a}{V^*}=\frac{6.37\times10^8 \text{ cm}}{2 \text{ cm sec}^{-1}}=8.7 \text{ yr}.$$

For purposes of scale analysis we neglect lateral gradients, and write the equation for apparent temperature in the form

$$\frac{\Delta\vartheta}{\Delta t}=-w\frac{\Delta\vartheta}{Z}+\frac{\Delta\vartheta}{Z^2}. \tag{4.14}$$

The first and second term on the right are the effects of vertical advection and diffusion, respectively. In the initial response to some change in boundary conditions, the term on the left would be of the same order as the terms on the right. Therefore, the time scale[1] given by (4.14) is Z^2. In the present numerical calculation, the temperature is calculated at six different levels, the vertical spacing of these levels and the time scale associated with each level being shown in Table 2.

[1] The authors are indebted to the reviewers for pointing out this time scale.

TABLE 2. The position of levels in the present numerical experiment and the adjustment time scale based on (4.14). The time scale in years is based on a rotation rate and scale velocity appropriate for the real ocean.

	Level					
	1	2	3	4	5	6
$-Z$	0.25	0.50	1.00	2.00	4.00	8.00
Δt	0.06	0.25	1.00	4.00	16.00	64.00
Years	½	2	9	35	139	557

Temperature differences tend to be very small at levels well below the thermocline. The deep part of the basin tends to be filled with water, the temperature of which is very close to the minimum temperature found at the surface in the vicinity of the north wall. In any case, Table 2 predicts that the small changes that do take place at lower levels will occur very slowly.

c. *Plan of the initial value calculation*

In order to keep the amount of calculation within reasonable limits the numerical integration is carried out in two stages. In the first stage the spacing of the numerical net is given by the curves labeled "A grid" in Fig. 3. The spacing is a little over 3° or 0.05 rad in each direction with a slightly finer spacing in the λ direction near the western boundary. The initial, horizontally uniform stratification is specified in Table 3.

Near the boundaries the vertical motion may be as much as one or two orders of magnitude larger than in the interior. From (4.14) it can be seen that such a large vertical motion leads to a very rapid response in the thermal field. For this reason the strong density gradients and associated currents appear at the boundaries long before the interior has come into adjustment. Since the total kinetic energy integral is largely a measure of the intensity of just the strongest currents, it reaches a level very near its maximum value very rapidly. This is shown in Fig. 4.

Note that the poleward heat transport fluctuates about a nearly steady value after about one unit of nondimensional time. This is an indication that poleward heat transport is largely determined by the upper part of the ocean as well as the lateral boundary regions. The general level of poleward heat transport is about 0.15 in units of $\theta^*\rho_0 c_p V^* ad$, where ad is a measure of the cross-sectional area. In the previous study A the heat transport was more nearly 0.3, but in that case the basin was nearly twice as wide.

TABLE 3. The initial, horizontally uniform distribution of apparent temperature.

	Level					
	1	2	3	4	5	6
$-Z$	0.25	0.50	1.00	2.00	4.00	8.00
ϑ	0.72	0.58	0.38	0.20	0.03	0.00

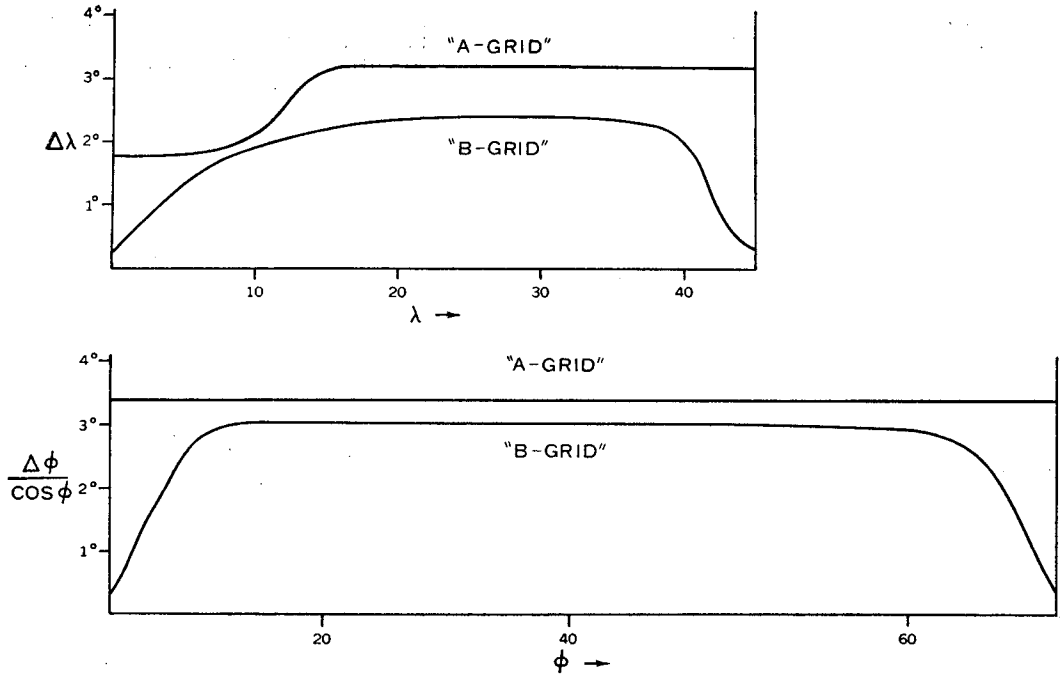

FIG. 3. Spacing of grid points in the horizontal plane. "A grid" refers to the net used in the first stage of the calculation; "B grid", the net used in the second.

Some insight into the adjustment of temperature over the basin during the first stage of the calculations is given by Fig. 5. The zonal average temperatures are plotted for levels 2, 4, 5 and 6. The scale has been expanded for the lower levels to show up the more subtle changes that take place there. It is interesting to compare the results given in Fig. 5 with the response times predicted in Table 2. The predicted response times at levels 2 and 4 are confirmed quite well in Fig. 5, while at level 5 the temperature appears to reach a steady value at closer to 10 units of time rather than the 16 predicted. The run is not long enough to get the full response at the bottom level. The results only confirm that the response time is longer than 22 units.

An interesting aspect brought out by Fig. 5 is that the isotherms at different latitudes change in a nearly parallel fashion, except at 45.6°. This means that in the southern portion of the basin the meridional temperature gradients are established quite early. The absolute value of the temperature continues to adjust itself, but the north-south gradient remains nearly constant. This is significant from a dynamic standpoint, since it is the lateral gradients of apparent temperature which are important in determining the velocity pattern.

At the end of the first stage of the calculation the fields are interpolated linearly from grid A to grid B shown in Fig. 3. The time integration is then extended for another unit of time. The behavior of the heat transport during this final stage of the run is shown in Fig. 6. The different types of time-dependent motions responsible for the fluctuations in heat transport during this second stage of the calculation are described in Part II. A profile of the western boundary current averaged over the interval shown in Fig. 6 is given in

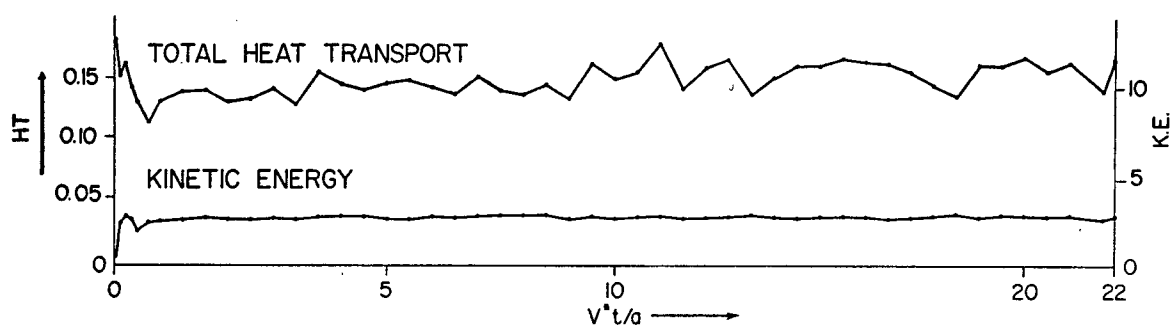

FIG. 4. The kinetic energy and poleward heat transport as a function of time during the first stage of the calculation. The ordinates are in nondimensional units.

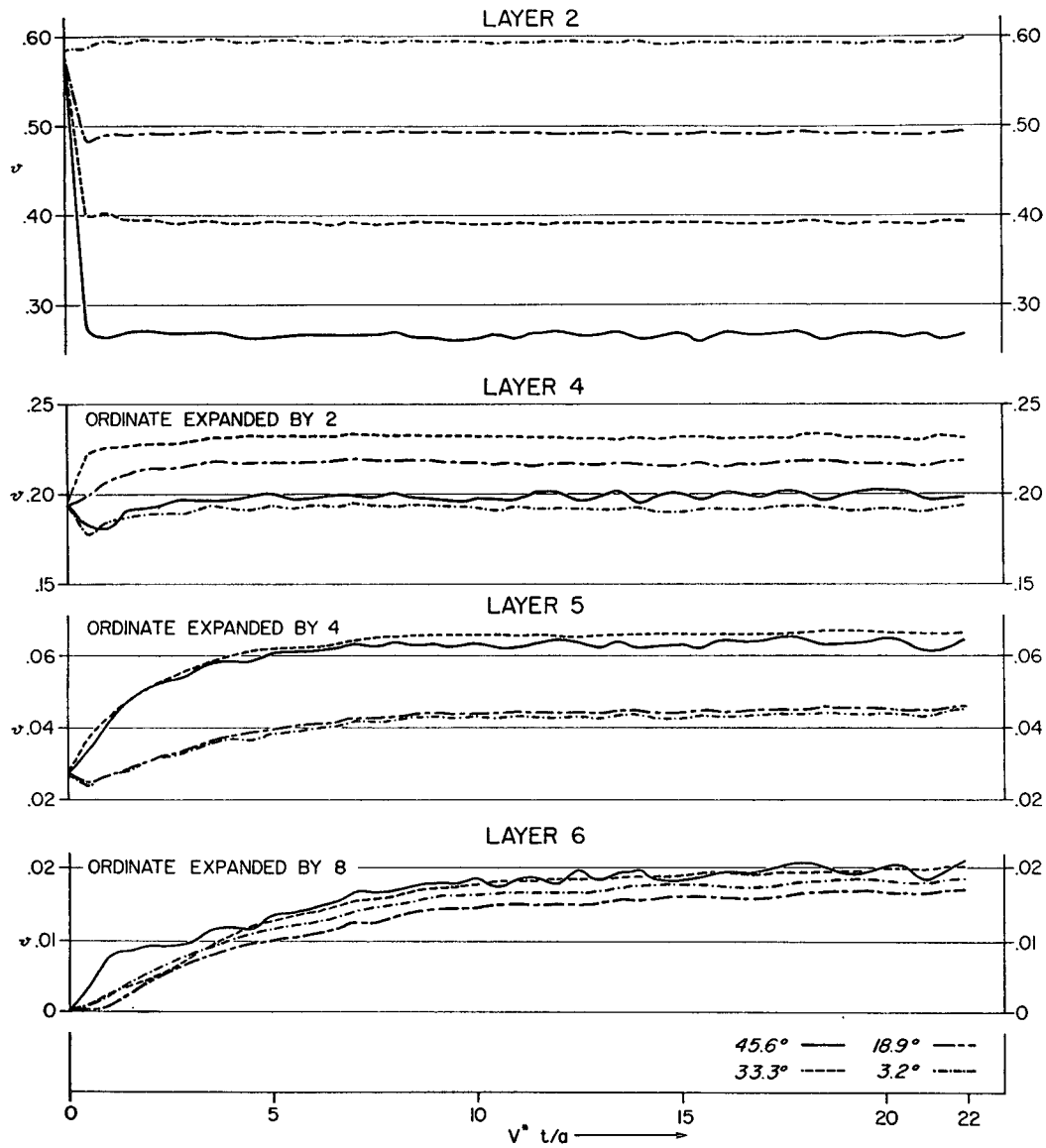

FIG. 5. Changes in the zonally averaged temperatures for different layers during the first stage of the calculation. Note the difference in response with respect to depth.

Fig. 7 as curve b, curve a being taken from the final part of the first stage of the calculation. Fig. 7 shows that the boundary current is adequately defined by the grid used in the second stage of the calculation.

d. Machine requirements

The calculations are carried out on a UNIVAC 1108 computer. The high speed drums on this machine make the calculations with large fields relatively easy. In the first stage of the calculation it is possible to integrate over one unit of nondimensional time in only 4256 time steps, each time step requiring 5.8 sec on the machine. In the final stage of the calculation 21,280 time steps were required to integrate over one unit of time. In this case each time step required 12.2 sec of machine time. The method of this study does have the disadvantage of requiring access to very powerful computing machines. If present trends in computer development continue, large computing requirements by present-day standards may appear in the future to be relatively modest.

5. The density and velocity fields

To orient the description of the solution with respect to previous studies, two important integrals of the velocity will be discussed. One such integral is the total

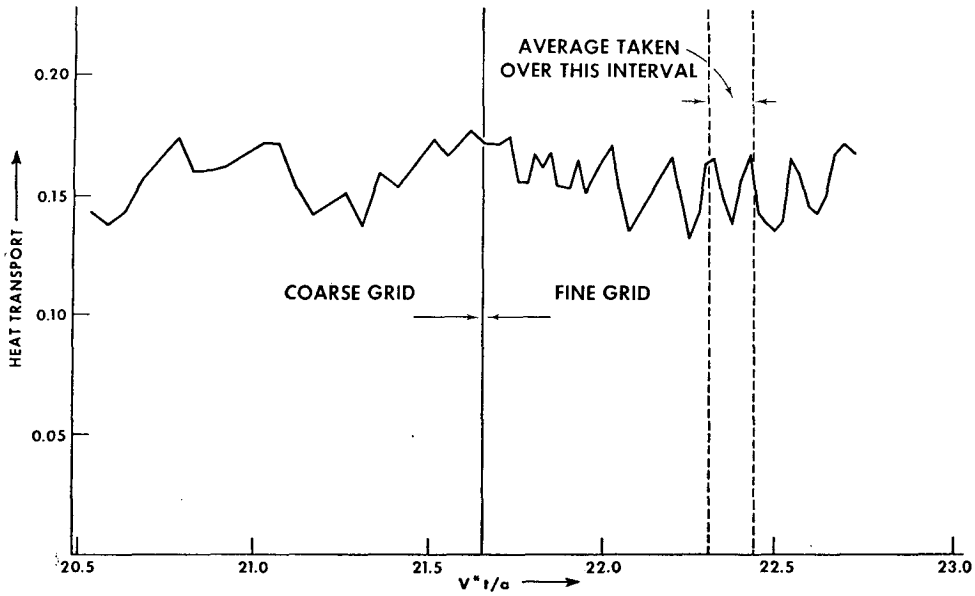

FIG. 6. The heat transport at 45° latitude showing the transition from stage 1 to stage 2 of the calculation. More details about the time dependent behavior will be given in Part II of this study.

mass transport in the horizontal plane. A transport stream function may be defined as

$$\psi_\lambda = \int_{-H/a}^{0} \rho_0 v \cos\varphi \, dz,$$

$$\psi_\varphi = -\int_{-H/a}^{0} \rho_0 u dz,$$

this function being the principal variable for which solutions are obtained in the theory of a wind-driven ocean. The pattern for the present baroclinic model is given in Fig. 8a. For the interior region, the general shape of the pattern could be predicted from the Stommel-Sverdrup theory. The wind stress specified at the surface shown in Fig. 1 exerts a counterclockwise torque at very low latitudes, a clockwise torque in the subtropical zone, and a counterclockwise torque at very high latitudes. Correspondingly, tropical and subtropical circulation gyres show up in the pattern of transport stream function, but no organized flow appears in the subarctic region. At the western boundary, however, the transport pattern is markedly different from the linear solution computed for the same geometry and wind stress distribution shown in Fig. 9. The linear solution indicates a symmetry in which the pattern of transport stream function at the western boundary is very much the same in regions of outflow as it is in regions of inflow. Inertial effects greatly alter this pattern so inflow spreads out along the boundary, and the outflow is concentrated into a rather narrow jet between the subtropical and subarctic gyre. Except for the disorganized time-dependent flow in the subarctic region, patterns similar to Fig. 8a have been obtained previously in the study of a nonlinear barotropic model by Bryan (1963). In the barotropic case, the numerical solution showed that the outflow took place almost exactly at the latitude separating the two wind gyres. On the other hand, the present baroclinic model shows an "overshoot" in which the outflow in Fig. 8a takes place 3–4° north of the boundary separating the wind gyres.

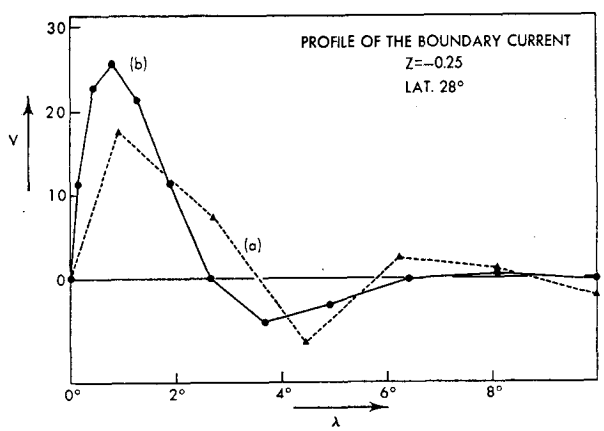

FIG. 7. Profiles of the western boundary current for the level nearest the surface. Curve (a) is the final result of the first stage of the calculations, (b), the average current in the second.

Munk (1950) suggested that with accurate estimates of wind stress over the North Atlantic and North Pacific, the total transport of the western boundary currents could be predicted quite accurately. This hypothesis has never been tested, since measurements of both transport and wind stress did not have the required accuracy. The transport of the boundary

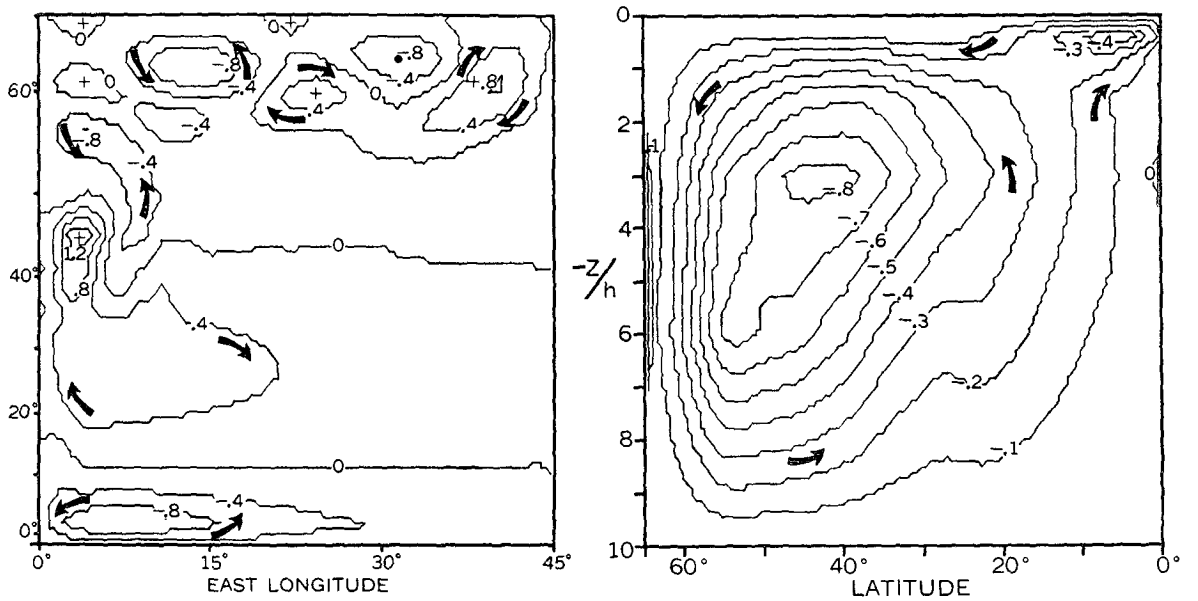

FIG. 8. Pattern of the total mass transport in the $\lambda = \varphi$ plane, a., the maximum transport being greater than 1.6 in the intense gyre near the western boundary at 48° latitude, and in the $\varphi = z$ plane, b. Both patterns must be multiplied by $V^*ad\rho_0$ to obtain the transport in dimensional units.

current must balance the interior flow. An expression for the transport in the linear case is obtained by integrating the Sverdrup transport given by (2.18b) across the basin, i.e.,

$$\int_{\lambda_1}^{\lambda_2}\int_{-H}^{0} \rho_0 va\cos\varphi\, dzd\lambda = -a(\tau^\lambda)_\varphi(\lambda_2-\lambda_1)/2\Omega, \quad (5.1)$$

where λ_1 and λ_2 are the longitudes of the west and east boundaries, respectively. Substituting from (2.18b) and (2.18c), an expression for the total Sverdrup transport is

$$\int_{\lambda_1}^{\lambda_2}\int_{-H}^{0} \rho_0 va\cos\varphi dzd\lambda = V^{**}\rho_0 da(\lambda_2-\lambda_1). \quad (5.2)$$

The nondimensional transport is obtained by dividing both sides of (5.2) by the scale transport, $V^*\rho_0 ad$. Thus,

$$\frac{1}{V^*\rho_0 ad}\int_{\lambda_1}^{\lambda_2}\int_{-H}^{0} \rho_0 va\cos\varphi dzd\lambda = \frac{V^{**}}{V^*}(\lambda_2-\lambda_1). \quad (5.3)$$

In the present case the basin is 0.8 rad wide. Since V^{**} has been chosen to be equal V^* (see Table 1), the total Sverdrup transport is 0.8.

The maximum transport shown in the linear solution of Fig. 9 corresponds very closely to this estimate. On the other hand, the nonlinear baroclinic case shown in Fig. 8a has a maximum of 1.5. An inertial amplification of transport is indicated here. This effect has already been demonstrated very clearly in barotropic solutions by Veronis (1966). On the basis of the present solution it appears that linear theory only provides a minimum estimate of the transport of the western boundary current.

After examining the transport component most closely connected with the wind-driven ocean circulation, we turn to the corresponding transport pattern in the north-south vertical plane, which is most closely

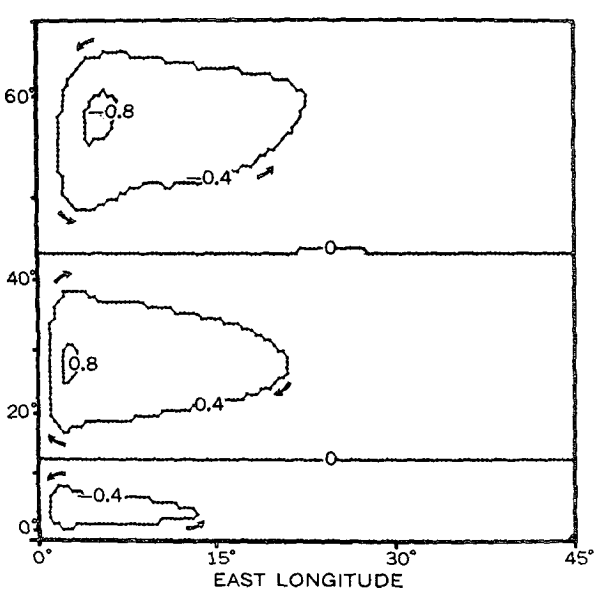

FIG. 9. Linear solution for a wind-driven ocean pattern of mass transport stream function corresponding to the nonlinear baroclinic case in Fig. 8a.

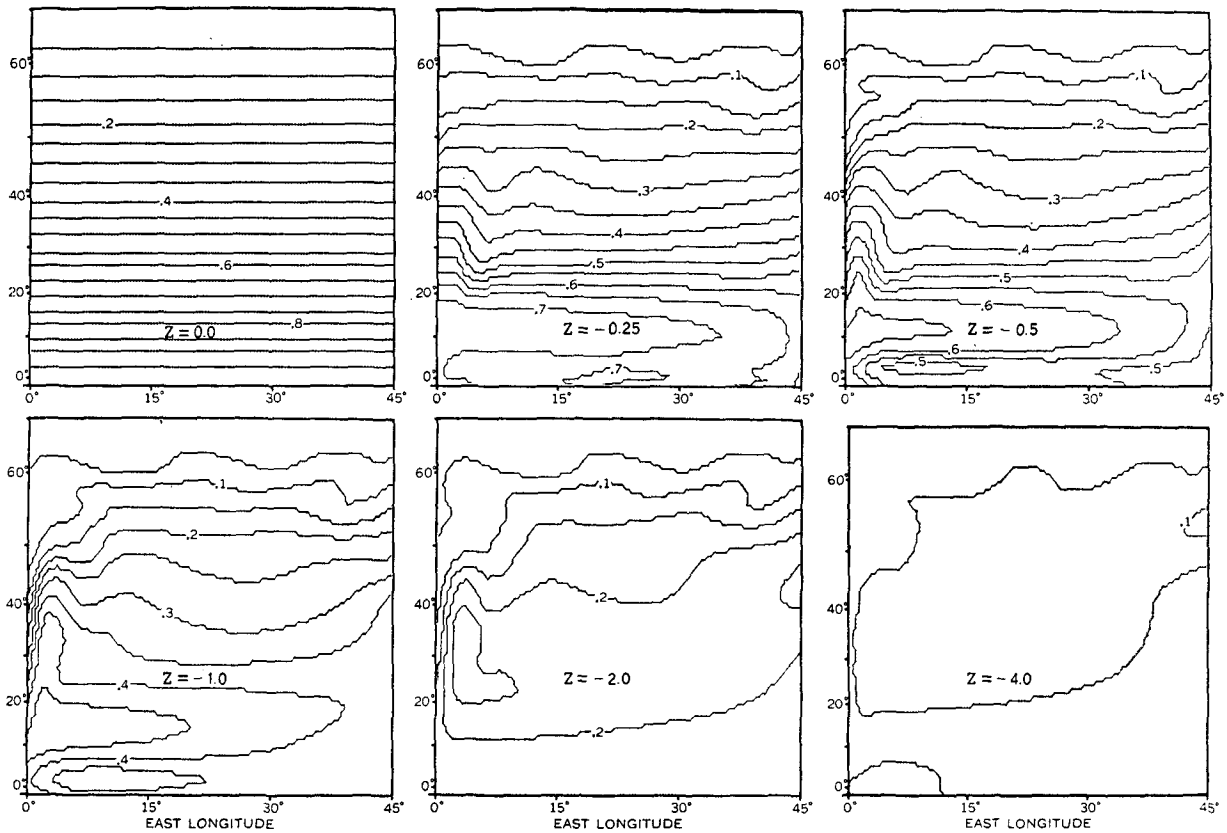

FIG. 10. Horizontal temperature patterns of the final solution. The pattern at $Z = 0.0$ is specified by the surface boundary condition.

connected with the thermohaline circulation. The pattern of the meridional mass transport is shown in Fig. 8b. Here the transport stream function is defined by

$$\psi_\varphi = -\int_{\lambda_1}^{\lambda_2} \rho_0 w \cos\varphi d\lambda,$$

$$\psi_z = \int_{\lambda_1}^{\lambda_2} \rho_0 v \cos\varphi d\lambda.$$

In the previous case integration is carried out with respect to the vertical. Here an integration is made with respect to longitude. The pattern of transport shows a concentrated downflow near the northern wall, and a very broad region of upward motion over the rest of the basin.

The small, nearly independent gyre at the surface in low latitudes will be described in more detail in Part II. It plays an important role in determining the velocity structure at the equator. A similar surface gyre is also indicated in study A. It is shown in A that this gyre does not form when the wind stress is absent at the surface. The results show that the main meridional overturning is density-driven, but the small surface gyre is primarily wind-driven.

In *The Gulf Stream*, Stommel estimates that the net overturning of the thermohaline circulation in the North Atlantic amounts to about 40 million tons, about the same magnitude as the horizontal mass transport of the western boundary current. In nondimensional units, the amplitude of the meridional circulation of Fig. 8b is shown to be 0.8, compared to the maximum amplitude of 1.5 in the same units for Fig. 8a. The present calculation, therefore, indicates a ratio of about 1:2 between the strength of the vertical overturning to the maximum strength of the western boundary current.

The apparent temperature patterns from the surface down to the 5th level are shown in Fig. 10. At the surface the temperature is a function of latitude only as specified by the boundary condition on temperature. The deviations from zonal symmetry which appear at $Z = -0.25$ are best developed in low latitudes. At higher latitudes, cooling at the surface leads to very strong convective mixing along the vertical coordinate. The result is to tie the temperature below the surface more closely to the pattern specified by the surface boundary condition. The wavy pattern at high latitudes is connected with the time-dependent eddies that show up in the transport pattern of Fig. 8a. The principal features of the thermocline configuration are best developed at $Z = -1.0$. A warm pool at the western side of the ocean is clearly shown. In addition, there is a warm

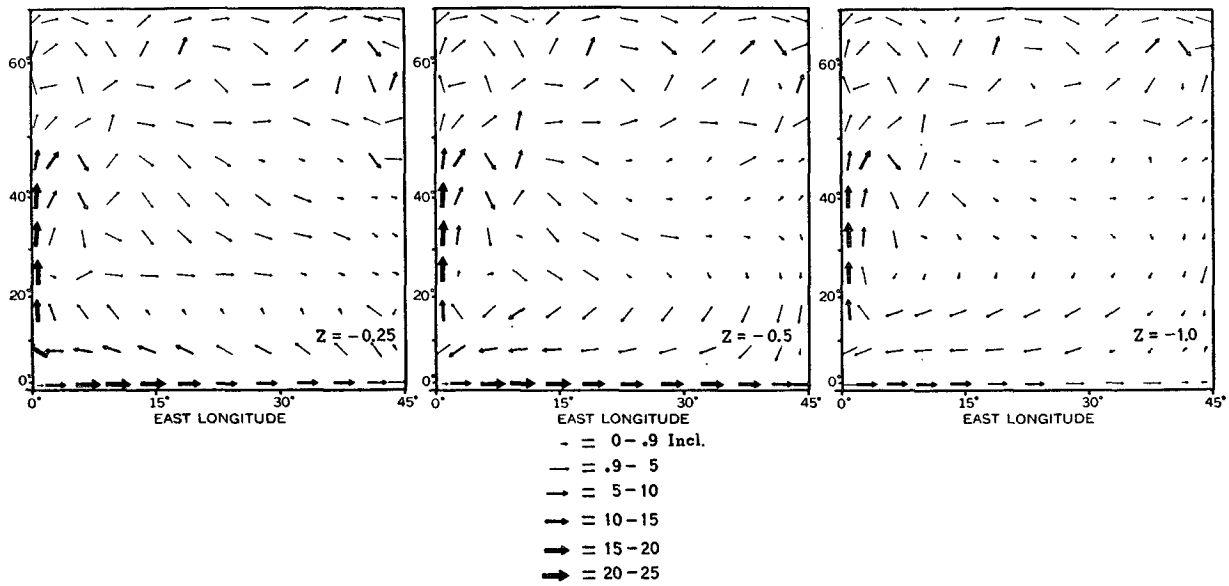

FIG. 11. Horizontal velocity vectors for levels 1–3, respectively.

tongue extending northward along the path of the western boundary current. Along the eastern wall downwelling at middle latitudes and upwelling at low latitudes may be inferred from warm and cold anomalies, respectively (also see Fig. 13). The inferred upwelling in the southeast corner of the basin appears to be an analogue to the upwelling observed off the coast of Africa and California.

At the 4th level ($Z=-2.00$) the temperature pattern is much weaker, but part of the warm tongue along the western boundary remains. A cold mass of water bulges out from the western wall at about 50N along the north side of the main outflow from the wall as shown in Fig. 8a. This feature may be related to the cold wedge of water in the North Atlantic trailing off to the southeast from the Grand Banks, documented in detail by Worthington (1962).

According to Worthington, the cold wedge in the North Atlantic separates the subtropical gyre from a smaller independent clockwise gyre to the north. Recent measurements indicate that during the southwest monsoon, a similar cold ridge on a somewhat smaller scale may exist in the Somali Current (Swallow and Bruce, 1966).

Since the horizontal velocity is strongly convergent and divergent near the boundaries, the velocity field cannot be accurately represented by a stream function. Therefore, vectors have been used to show the equilibrium fields in Figs. 11 and 12. To avoid crowding, vectors have only been plotted at alternate grid points in the north-south and east-west direction in the vicinity of the western boundary. The flow in the upper 3 levels shown in Fig. 11 is basically the same. Strong currents are located at the western boundary and along the equator. A comparison of the results for different levels shows that the current at the equator is much shallower than the western boundary current. At the eastern wall, the flow to the east has even reversed at the 3rd level below the surface. Note that the flow at level 1 is northward everywhere along the western boundary except very close to the equator. The flow is quite different from what would be predicted on the basis of the pattern of total mass transport given in Fig. 8a. Between 45 and 50N, the western boundary current greatly diminishes in intensity. The outflow from the wall splits into two branches, some continuing northeastward, and some going into a lateral countercurrent flowing southward. Note that the weak northeastward flowing branch tends to make a counterclockwise recurvature back to the western wall. This velocity pattern appears to be closely associated with the cold wedge evident at $Z=-2.0$ in Fig. 10.

Eastward drift takes place over the entire northern part of the basin at upper levels, while flow to the west is confined to the tropics south of 20N. At the level nearest the surface ($Z=-0.25$) there is a strong drift away from the equator, except at the western wall. This is largely Ekman drift caused by the surface stress pattern. The surface drift away from the equator is largely compensated by a southward drift in the layer just below. This pattern shows up very clearly in the meridional circulation diagram shown in Fig. 8b.

The circulation pattern at lower levels is shown in Fig. 12. At the $Z=-2.0$ level, departures from the upper level flow are just beginning to show up. At the equator, flow is to the west rather than to the east. The strong current at the equator is much shallower than the western boundary current.

Much greater departures from the surface flow show up at $Z=-4.0$ and $Z=-8.0$. Over the whole basin

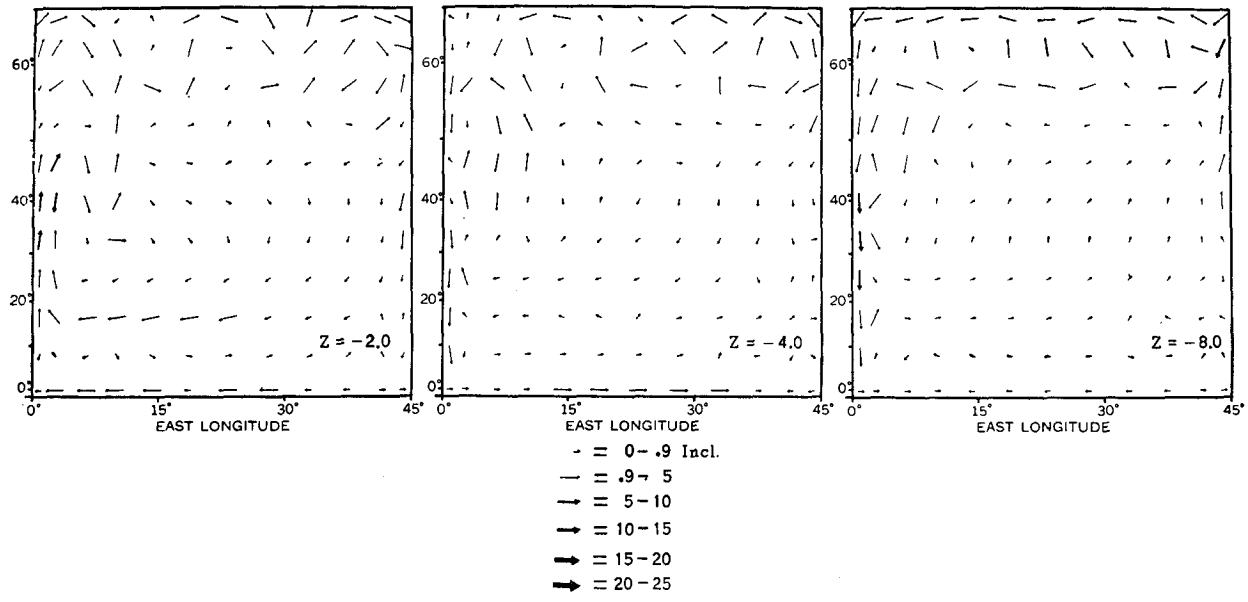

FIG. 12. Horizontal velocity vectors for levels 4–6, respectively.

the abyssal circulation is predominantly counterclockwise, and accords very well with the simplified two-layer solution of the thermohaline circulation given by Stommel (1965, p. 160). An intense southward flow occurs at the western boundary underneath the western boundary current, and gentle northward drift occurs in the interior. Other features of the abyssal flow which are unique include a continuous westward flow along the northern wall fed by strong sinking in the northeast corner.

Oceanographic observations only provide very indirect clues concerning vertical motion. In addition, the pattern of vertical motion is extremely difficult to predict for a rotating fluid by ordinary physical reasoning. Therefore, the vertical velocity components given by the solution are of special interest. Fig. 13 shows

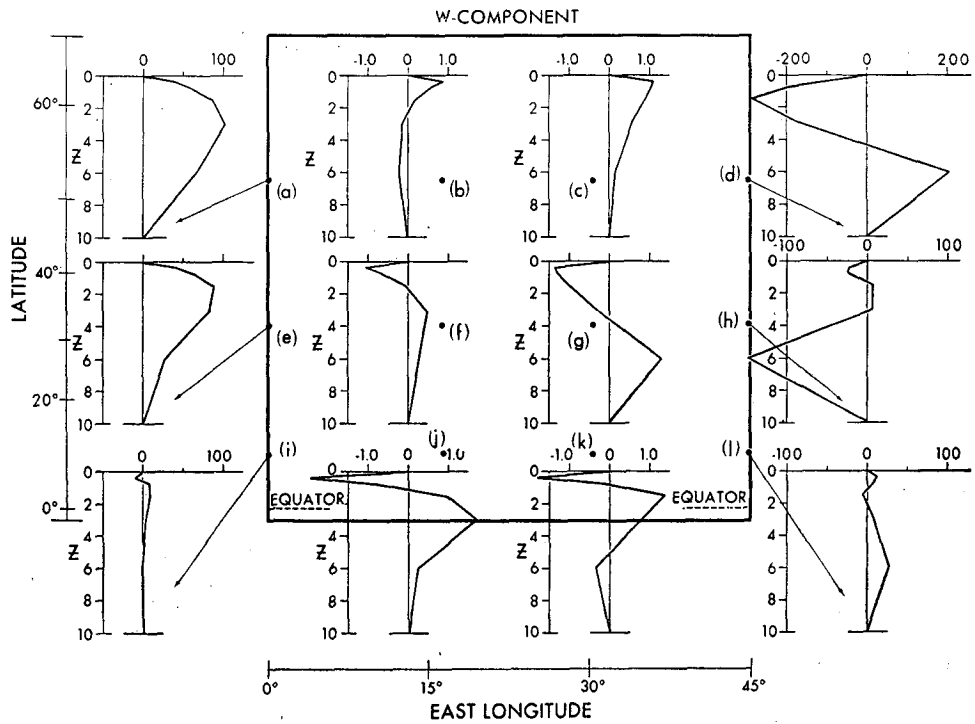

FIG. 13. Vertical profiles of the w component. Position is indicated by the heavy dots within the outline of the basin. Note the scale of the abscissa is greatly expanded for interior points.

the vertical profiles of the w component for 12 different points in the basin. Half of the points are in the interior, and the other half are located just adjacent to the lateral boundaries.

The interior profiles (f), (g), (j) and (k) of Fig. 13 in the tropics and the subtropics are basically similar. Sinking occurs at the surface with rising motion at mid-levels. In the subtropical gyre, sinking extends to much lower levels than in the tropics. The deep pool of warm water that results from this downward motion forced by the convergence of the Ekman drift has already been pointed out in connection with the temperature patterns of Fig. 10.

The vorticity equation is a very useful tool in relating the vertical motion to other features of the velocity field. If (2.24) is multiplied by $\cos\varphi$ and differentiated with respect to φ, and the result subtraced from (2.25) differentiated with respect to λ, we have

$$\begin{aligned}\mathrm{Ro}[Dv+\tan\varphi\, uu-v_{zz}]_\lambda \\ -\mathrm{Ro}[\cos\varphi(Du-\tan\varphi\, uv-u_{zz})]_\varphi \\ +v\cos^2\varphi-w_z\sin\varphi\cos\varphi \\ =\mathrm{RoRe}^{-1}[F_\lambda{}^\varphi-(\cos\varphi\, F^\lambda)_\varphi]. \quad (5.4)\end{aligned}$$

Dropping all terms of O(Ro) or less in (5.4) and integrating with respect to z,

$$w(z)=\int_{-H/d}^{z}\frac{v\cos\varphi}{\sin\varphi}dz. \quad (5.5)$$

As indicated by Fig. 12 the abyssal flow is northward over most of the basin. Following the argument given by Stommel (1965, p. 153), this northward flow is consistent with general upwelling at the base of the thermocline in the subtropical gyre. As indicated by (5.5) the maximum value of w corresponds to the level of no meridional motion.

The marked contrast between the vertical velocity profiles (b) and (c) of Fig. 13 may also be explained in terms of the differences in the meridional flow in the western part of the subarctic zone, and very weak meridional flow in the vicinity of (c). Correspondingly strong downwelling occurs at (b), but not at (c). The pattern of wind stress implies a divergence of Ekman drift in the subarctic gyre. Consequently, both points show upwelling right at the surface, in contrast to the downwelling at the surface in the subtropical zone.

The pattern of vertical velocity along the lateral boundaries is more complicated. We see that very strong upwelling takes place all along the western boundary except right at the surface in the tropics. Evidence that the simple relation (5.5) no longer applies at the wall is given at point (e). Upwelling is strong at lower and middle levels even though a strong southward flowing undercurrent is present at the wall. In Part II of this paper the vorticity balance in the western boundary current is analyzed in detail. It will be shown that close to the wall ageostrophic terms have the same magnitude as the geostrophic terms. In particular, lateral friction and inertia terms balance the divergence terms, leading to the strong upwelling right at the wall.

Along most of the eastern wall, downwelling takes place to absorb the strong inflow connected with the general eastward drift at the surface. Only in the tropics is the situation reversed. There an upwelling is required to maintain the offshore flow in a westward current, corresponding to the North Equatorial current. As indicated by Fig. 10, this upwelling is highly significant in changing the temperature patterns due to the strong vertical stratification at low latitudes.

Up to this point only patterns of velocity and temperature in the horizontal plane are examined. While these patterns are sufficient to show most features of the flow, additional insight can be gained by examining vertical cross sections. This form is more convenient to compare with actual observations, since oceanographic data is usually presented this way.

First, three meridional sections of apparent temperature at different longitudes are shown in Fig. 14, the patterns being very similar. Greater differences might

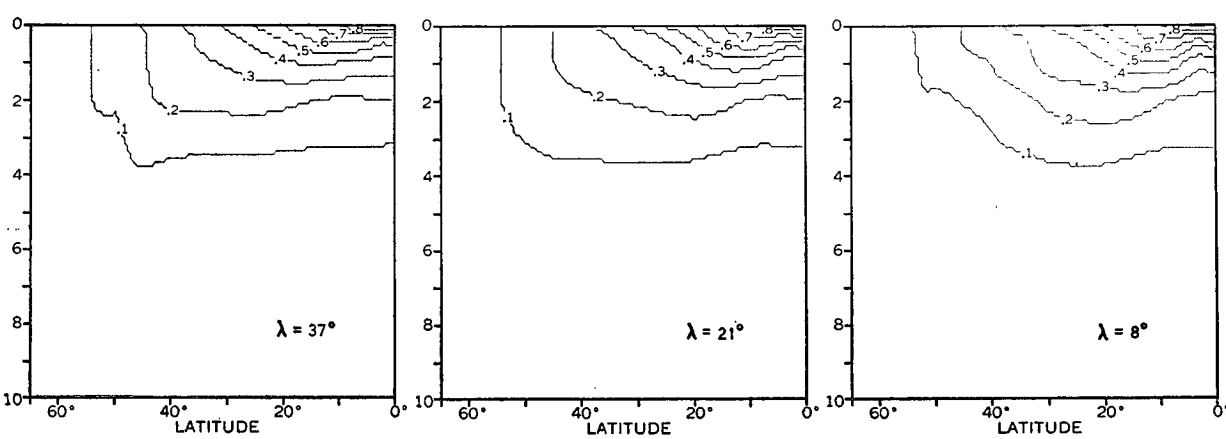

FIG. 14. Meridional cross sections for temperature. Very strong upwelling in the tropics and convective mixing in the subarctic region are indicated.

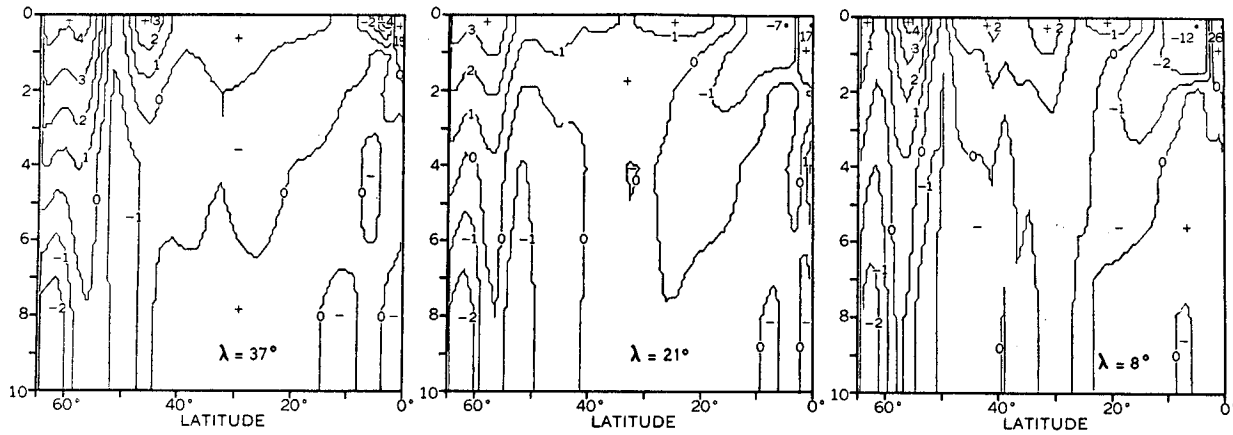

FIG. 15. Meridional cross sections corresponding to Fig. 14, but showing the u component of velocity.

be expected if it were not for the zonally symmetric boundary condition imposed on the temperature at the surface. The stratification becomes shallower and more intense in low latitudes. This effect has previously been reproduced in the thermocline theories of Robinson and Stommel (1959) and Welander (1959). A simple interpretation in terms of a vorticity argument has been given by Phillips (1963). For very slow motion in the ocean it might be expected that potential vorticity would be approximately conserved along trajectories. For low Rossby number flow the relative vorticity term can be neglected, and we have

$$\frac{d\rho}{dz}\sin\varphi = \text{constant}. \tag{5.6}$$

In the case of weak mixing, trajectories should approximately coincide with isothermal surfaces. To test how well this idealized formula fits the present solution, the quantity $\sin\varphi/\Delta z$, where Δz refers to the vertical distance between specific pairs of isotherms, is given in Table 4. Values have been picked off the temperature cross section in Fig. 14 for $\lambda = 21°$. The thermal structure shows fair agreement with the absolute potential vorticity conservation law for the region from 20°–40° of latitude. The reason for the discrepancies at 10° is not clear.

TABLE 4. Values of the sine of the latitude divided by the depth interval between isotherms vs φ, taken from Fig. 14, for $\lambda = 21°$. This quantity is a measure of the absolute potential vorticity.

Isotherm interval	Latitude 10°	20°	30°	40°
0.6–0.5	0.86			
0.5–0.4	0.47	0.70		
0.4–0.3	0.43	0.56	0.61	
0.3–0.2	0.38	0.34	0.38	
0.2–0.1	0.13	0.33	0.35	0.36

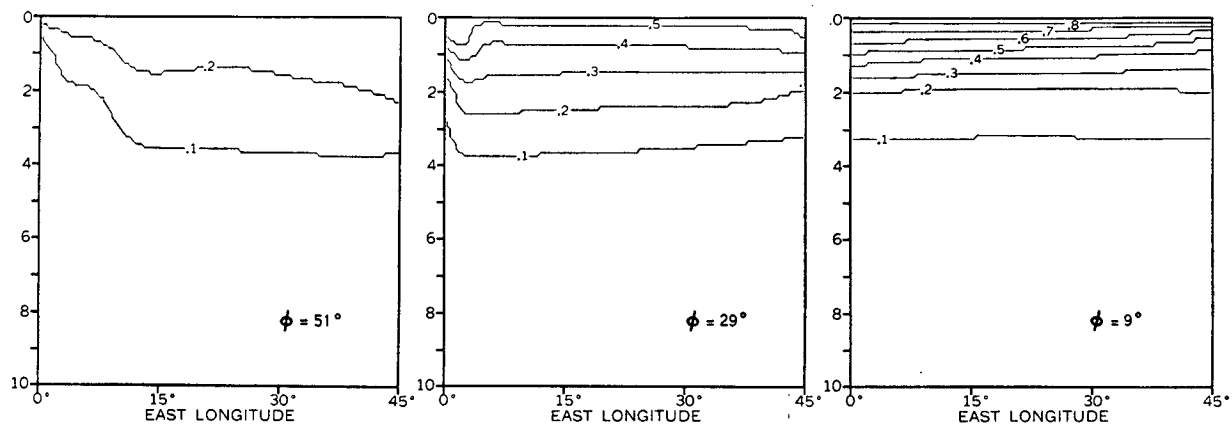

a. b. c.

FIG. 16. East-west temperature cross sections for the subarctic, a., the subtropics, b., and the tropics, c.

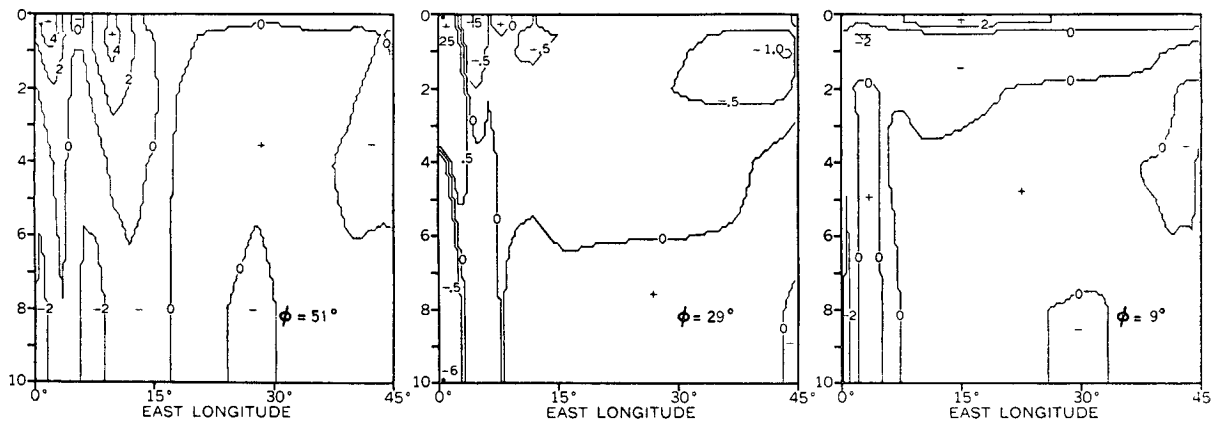

FIG. 17. East-west cross sections of the meridional velocity corresponding to the temperature sections of Fig. 16.

The zonal flow is shown in Fig. 15 in three sections which correspond to the previous temperature sections. These sections show interesting differences in the vertical penetration of various currents. Where isotachs would have been too congested they have been omitted, and only the maximum or minimum value is given. The location of the maximum or minimum is designated by a solid black dot. At the surface the counterpart of the equatorial undercurrent and the equatorial countercurrent show up in the tropics of all three sections. Both are shallow compared to the currents at higher latitudes. Note that the complex eastward drift at middle latitudes extends down to the bottom in some places.

Three vertical east-west sections of apparent temperature are shown in Fig. 16. General features of the North Atlantic thermocline structure are recognizable. In the subarctic zone the isotherms slope downward to the east, while in the subtropical zone they slope upward towards the east, except at the surface. At midlatitudes a sharp gradient is present at the western boundary, associated with the western boundary current. At $\varphi=9°$ Fig. 16 shows that the thermocline is nearly flat and very shallow.

The vertical cross sections of the v component of velocity which correspond to the temperature sections are given in the next figure. Starting with the subarctic section in Fig. 17, we note that over most of the lower part of the section, a counterclockwise circulation exists with northward flow to the east and strong southward flow along the western boundary. Right at the surface, however, the sense of circulation is reversed and a shallow clockwise circulation is present.

As noted previously, the subtropical section shows a highly organized flow that conforms very well with Stommel's (1965, p. 160) predictions of the deep ocean circulation. Both the abyssal and surface flow show strong western intensification. Details of the boundary current will be discussed in connection with Fig. 18.

The meridional flow in the tropics is much more complex. The shallow northward drift right at the surface has been discussed in connection with Fig. 11. This is underlaid by a geostrophic flow toward the equator. The southward flow forms a shallow continuation of the southward drift in the subtropical gyre. At greater depths, the abyssal currents are weak and disorganized.

A comparison of the Gulf Stream with the computed western boundary current is afforded by Fig. 18. A marked difference exists in the horizontal scale of the two figures, but a careful examination shows that the computed current is about 3° wide. On the other hand, the observed width according to Swallow and Worthington (1961) is about 1° of longitude. The simplified scale theory of the preceding section indicates that for an inertial current, the width should be proportional to $\mathrm{Ro}^{\frac{1}{3}}$. Tables 1 and 2 indicate that the present value of Ro equal to 2×10^{-4} is about an order of magnitude greater than an appropriate one for the real ocean. Using (3.3) this would correspond to a factor of 3.2 difference in width of the boundary current. The result is not inconsistent with Fig. 18.

With respect to velocity, one would expect that increased width is associated with a slower current. In order to make a comparison the maximum speed of the calculated boundary current should be multiplied by a factor of $\sqrt{10}$ or 3.2. This gives a velocity of 77 nondimensional units. Based on the parameters given in Section 4b an appropriate scale velocity V^* for the real ocean is about 2 cm sec^{-1}. Thus, the calculated current maximum would correspond to 154 cm sec^{-1}, compared to the observed velocity maximum of 180 cm sec^{-1}, a discrepancy of about 15% being indicated.

A similar comparison between the computed pattern of the equatorial current and observation is allowed by Fig. 19. The computed pattern on the left shows the zonally averaged pattern of the u component. The

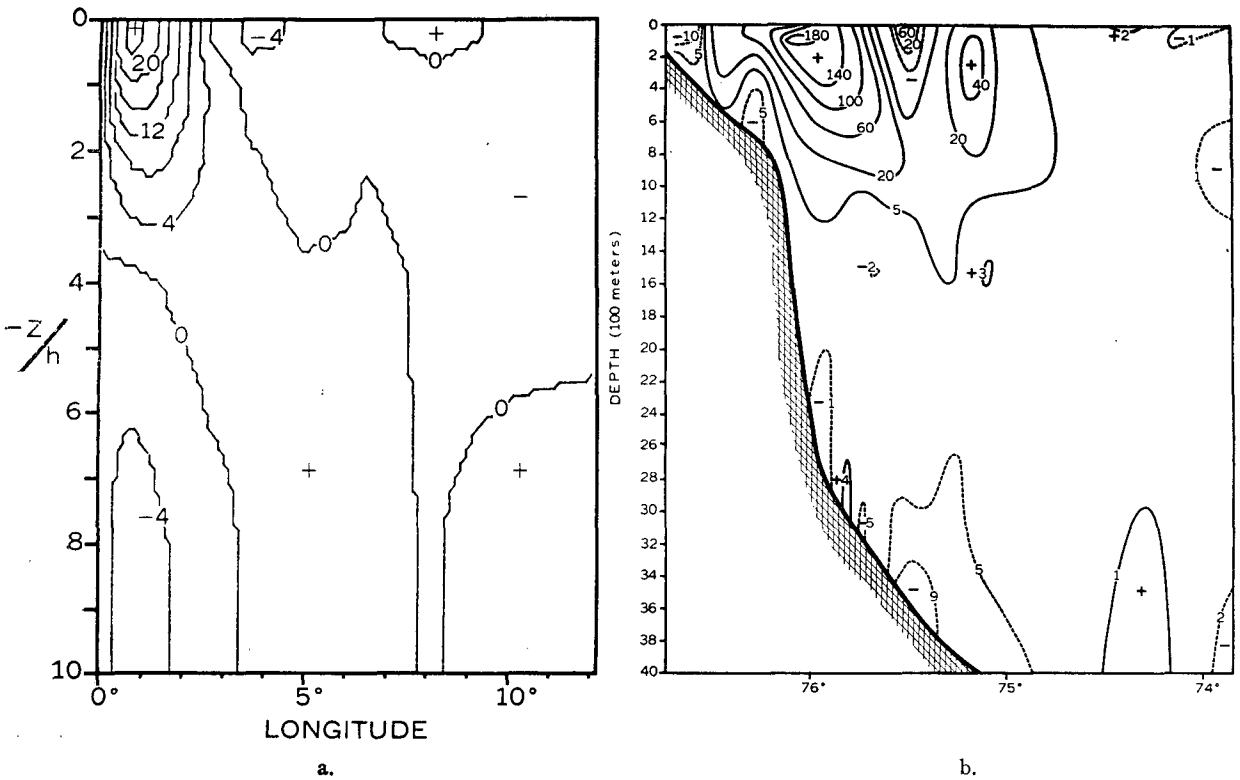

FIG. 18. Computed western boundary current at a latitude of 28°, given in nondimensional units, a., and observed profile of the Gulf Stream off Cape Hatteras given by Swallow and Worthington (1961), b. Units are cm sec^{-1}.

computed pattern is based on velocity values at levels placed −0.25, −0.50 and −2.00 units below the surface. The resolution is not good enough to make details in the computed pattern significant. For example, it is not possible to determine whether detailed vertical resolution in the numerical net would allow a reversal of flow in the surface layer. In Fig. 19 velocities computed at the top level are simply extrapolated to the surface. The width of the computed current is 3.5° compared to an average width of about 1.5° in the

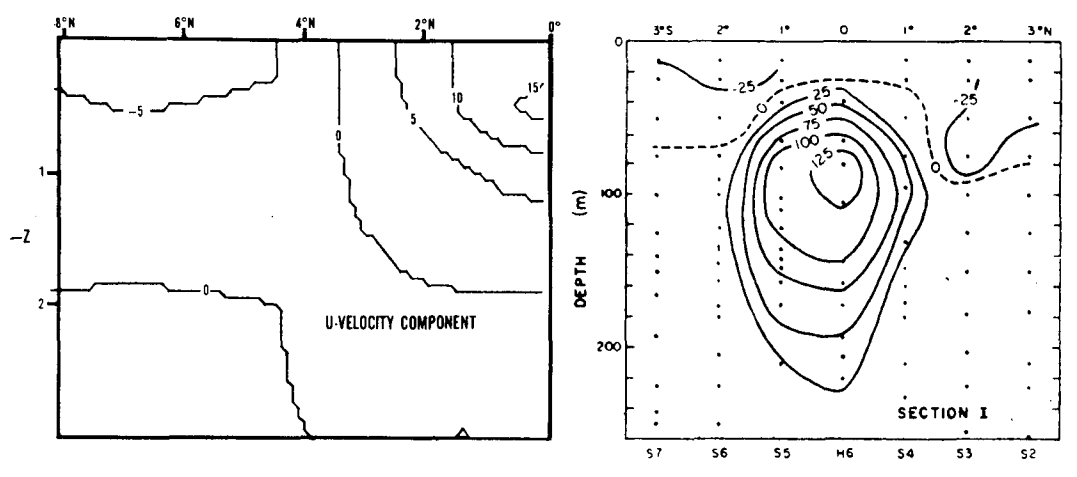

FIG. 19. The zonally averaged u component of the velocity in nondimensional units, a., and the Pacific Equatorial Undercurrent at 140W (Knauss, 1960), b. Units are cm sec^{-1}.

observed pattern on the right. If the maximum velocity of 15 units is multiplied by the same factor, $V^*\sqrt{10}$, used in the case of the western boundary current, the result is 96 cm sec^{-1}. This is about 75% of the observed maximum shown on the right.

6. Summary

In order to establish a basis for further work, a single numerical solution of an ocean circulation model is described in detail. Symmetry is assumed to exist at the equator and the basin is bounded laterally by two meridians 45° apart. The basin extends to a latitude of 67°, and is of uniform depth. The circulation is driven by a north-south temperature gradient imposed at the upper boundary and by a pattern of wind stress similar to that observed over the real ocean. The solution is obtained by an extended numerical integration of the time-dependent equations.

Many features of the thermocline and circulation structure, which have been individually studied in previous investigations, are included in a single solution computed on the basis of very simple and straightforward boundary conditions. The thermal structure is very similar to that found in a previous study by the authors. A higher effective Reynolds number for the lateral turbulent viscosity permits a much greater role for the nonlinear terms in the vicinity of the western boundary current. The solution confirms two interesting results concerning nonlinear western boundary currents, which up to now have been based solely on barotropic models. One of these results (Bryan, 1963) is that inertial effects concentrate the outflow between the subtropical and subarctic circulation gyres into a relatively narrow jet.

The second result, first obtained in solutions for a barotropic model by Veronis (1966), is that inertial effects produce a recirculation associated with a lateral countercurrent which may amplify the mass transport of the western boundary current by as much as a factor of 2.

In addition to the western boundary current, a strong jet occurs along the equator. The intensity is very much the same as the western boundary current, but it tends to be much shallower.

No tendency was found for the time dependent motions in the solution to damp with increasing time, and it appears likely that a stable steady state does not exist in the present case. More details on the time dependent motion are given in Part II.

Acknowledgments. The authors have received a great deal of help from Miss Martha Jackson, Mrs. James Bunce, Mrs. Reginald Simpson, and Mrs. Rose Hudson in preparing the diagrams and typing the manuscript. For assistance in making the calculations, the authors also thank Mr. Howard Engelbrecht and his entire computer staff at the Geophysical Fluid Dynamics Laboratory. Helpful discussions with Syukuro Manabe, William Holland, Isidoro Orlanski, and Adrian Gill are sincerely appreciated.

APPENDIX

Finite Difference Treatment of the Planetary Boundary Layer

The numerical errors involved in calculating upwelling and the lateral advection of heat in the top layer of the numerical model are examined in this appendix. In particular, we consider the case in which the planetary frictional boundary layer is much less than the thickness of the top layer. Errors are estimated by determining the integrated values of the drift current and the advection of heat by the drift current from the Ekman theory. The results are then compared to what would be calculated with the finite difference method for the same case.

Consider the drift current governed by the equation

$$2id_E^{-2}q = q_{zz}, \tag{A.1}$$

where $q=u+iv$ and the Ekman depth is defined as $d_E=(\kappa/\Omega n)^{\frac{1}{2}}$. We let the boundary conditions on (A.1) be

$$\kappa q_z = \tau^*/\rho_0, \quad z=0,$$
$$q=0, \quad z=-\infty.$$

The solution for the drift current is then

$$q=(1-i)\tau^*(d_E/2\kappa\rho_0)e^{(1+i)z/d_E}. \tag{A.2}$$

If we now let Δz be the thickness of the top layer, the total transport of the drift current in this layer is

$$\int_{-\Delta z}^{0} q\,dz = -i\tau^* d_E^2/2\kappa\rho_0 + \cdots O(e^{-\Delta z/d_E}). \tag{A.3}$$

The finite difference equation corresponding to (A.1) is

$$2id_E^{-2}(\Delta z)^2 q_k = q_{k-1} - 2q_k + q_{k+1}. \tag{A.4}$$

As a simplification we will consider only a uniform spacing of grid points with respect to depth with the boundary conditions, i.e.,

$$\left.\begin{aligned} q_0 - q_1 &= \tau^*\Delta z/\kappa\rho_0, & k&=1 \\ q_k &= 0, & k&\text{ large}\end{aligned}\right\}. \tag{A.5}$$

Substituting (A.5) into (A.4), we find the drift transport in the top layer to be

$$q_1\Delta z = -i\tau^* d_E^2/2\kappa\rho_0 + \cdots O(d_E/\Delta z)^2. \tag{A.6}$$

In the case $\Delta z \gg d_E$ the total drift transport in the top layer is nearly the same in the finite difference solution (A.6) as in the continuous case (A.3). Errors in the total transport calculated by (A.6) will increase toward the equator, since the Ekman depth is inversely proportional to $(\sin\varphi)^{\frac{1}{2}}$. For the parameters used in the present calculation the difference between (A.3) and (A.6) at 20° away from the equator would be less than 1%, while at 5° away from the equator the error would be nearly 4%.

Errors in the computation of the lateral advection of heat by the drift current in the top layer are more serious. As indicated in Section 3 averages of products in the equations are approximated by the product of averages. For example,

$$\frac{1}{\Delta z}\int_{-\Delta z}^{0} \mathbf{q}\nabla\vartheta dz \rightarrow \mathbf{q}_1\nabla\vartheta_1, \tag{A.7}$$

where $\mathbf{q}_1$ and $\Delta\vartheta_1$ are averages of the horizontal velocity and the horizontal gradient of heat in the top layer. To calculate the error in the approximation (A.7), we must consider a specific temperature distribution. Suppose that a temperature gradient imposed at the surface decreases linearly with depth and in proportion to $\gamma/\Delta z$; that is,

$$\nabla\vartheta = G^*(1+\gamma z/\Delta z). \tag{A.8}$$

For $\gamma=1$ the surface temperature gradient would go to zero at the base of the top layer.

Substituting (A.2) and (A.8) for $\mathbf{q}$ and $\nabla\vartheta$ in the left-hand side of (A.7), we obtain

$$\frac{(1-i)\tau^* d_E G^*}{2\kappa\Delta z\rho_0}\int_{-\Delta z}^{0}(1+\gamma z/\Delta z)e^{(1+i)z/d_E}dz$$

$$= -\frac{i\tau^* d_E^2 G^*}{2\kappa\Delta z\rho_0}[1-(1-i)\gamma d_E/2\Delta z]$$

$$+\cdots O(e^{-\Delta z/d_E}), \tag{A.9}$$

while the right-hand side of (A.7) may be obtained by integrating (A.2) and (A.8) separately and multiplying the integrals together, i.e.,

$$\frac{(1-i)\tau^* d_E G^*}{2\kappa(\Delta z)^2\rho_0}\left[\int_{-\Delta z}^{0}\left(1+\frac{\gamma z}{\Delta z}\right)dz\right]$$

$$\times\int_{-\Delta z}^{0} e^{(1+i)z/d_E}dz = -i\tau^* d_E^2 G^*(1-\gamma/2)/(2\kappa\rho_0\Delta z)$$

$$+\cdots O(e^{-\Delta z/d_E}). \tag{A.10}$$

The final result gives the ratio of the right- and left-hand sides of (A.7) as

$$\mathbf{q}_1\nabla\vartheta_1 \Big/ \left(\frac{1}{\Delta z}\int_{-\Delta z}^{0}\mathbf{q}\nabla\vartheta dz\right) = \frac{1-\gamma/2}{1-(1-i)\gamma d_E/2\Delta z}. \tag{A.11}$$

The error depends on the parameter γ. In the continuous solution the advection by the drift current is concentrated near the surface where the horizontal temperature gradient is largest. The finite difference method may be interpreted physically as smearing out the effect of the drift current throughout the entire depth of the top layer. The result is a serious underestimate of advection by the drift current if the horizontal temperature gradient decreases rapidly below the surface. For example, if the temperature gradient imposed at the surface goes to zero at the base of the first layer, the error will be about 50%. If the horizontal gradient is only reduced by one-half at the base of the first layer, the error is 25%.

REFERENCES

Arakawa, Akio, 1966: Computational design for long-term numerical integration of the equations of fluid motion: Two-dimensional incompressible flow. Part I. *J. Computational Phys.*, **1**, 119–143.

Bryan, K., 1963: A numerical investigation of a nonlinear model of a wind-driven ocean. *J. Atmos. Sci.*, **20**, 594–606.

——, and M. D. Cox, 1967: A numerical investigation of the oceanic general circulation. *Tellus*, **19**, 54–80.

——, and ——, 1968: A nonlinear model of an ocean driven by wind and differential heating: Part II. An analysis of the heat, vorticity and energy balance. *J. Atmos. Sci.*, **25**, 968–978.

Fischer, G., 1965: On a finite difference scheme for solving the nonlinear primitive equations for a barotropic fluid with an application to the boundary current problem. *Tellus*, **17**, 405–412

Fofonoff, N. P., 1962: Dynamics of ocean currents. *The Sea*, Vol. I, New York and London, J. Wiley & Sons, 864 pp.

Gormatyuk, Yu. K., and A. S. Sarkisyan, 1965: Results of 4-level model calculations of North Atlantic Currents. *Izv. Atmos. Oceanic Phys.*, **1**, 313–326.

Knauss, J. A., 1960: Measurements of the Cromwell current. *Deep-Sea Res.*, **6**, 265–286.

Munk, W., 1950: On the wind-driven ocean circulation. *J. Meteor.*, **7**, 79–93.

Phillips, N. A., 1956: The general circulation of the atmosphere: A numerical experiment. *Quart. J. Roy. Meteor. Soc.*, **82**, 132–164.

——, 1963: Geostrophic motion. *Rev. Geophys.*, **1**, 123–176.

Robinson, A. R., and H. Stommel, 1959: The oceanic thermocline and the associated thermohaline circulation. *Tellus*, **11**, 295–308.

Saint-Guilly, B., 1956: Sur la theorie des courants marins induits par le vent. *Ann. Inst. Ocean. (Paris)*, **33**, 1–64.

Sarkisyan, A. S., 1954: The calculation of stationary wind currents in the ocean. *Izv. Akad. Nauk (SSSR) Ser. Geofiz.*, **6**, 554–561.

——, 1962: On the dynamics of the origin of wind currents in the baroclinic ocean. *Okeanologia*, **11**, 393–409.

Smagorinsky, J., 1963: General circulation experiments with the primitive equations. *Mon Wea. Rev.*, **91**, 99–164.

Stommel, H., 1965: *The Gulf Stream, a Physical and Dynamical Description*. 2nd ed., Berkeley, University of California Press, 240 pp.

Swallow, J. C., and L. V. Worthington, 1961: An observation of a deep counter-current in the western North Atlantic. *Deep-Sea Res.*, **8**, 1–19.

——, and J. G. Bruce, 1966: Current measurements off the Somali coast during the southwest monsoon of 1964. *Deep-Sea Res.*, **13**, 861–888.

Veronis, G., 1966: Wind-driven ocean circulation, Part I and Part II. *Deep-Sea Res.*, **13**, 17–55.

Welander, P., 1959: An advective model of the ocean thermocline. *Tellus*, **11**, 309–318.

Worthington, L. V., 1962: Evidence for a two gyre circulation system in the North Atlantic. *Deep-Sea Res.*, **9**, 51–67.